AGU PUBLICATIONS

Geochemistry, Geophysics, Geosystems

RESEARCH ARTICLE
10.1002/2017GC007034

Special Section:
Wilson Cycles and the Formation of Marginal Basins: Rifting Dynamics and Mantle Evolution from Mid-ocean Ridge Creation to Extinction

Postseafloor Spreading Volcanism in the Central East South China Sea and Its Formation Through an Extremely Thin Oceanic Crust

Minghui Zhao[1], Enyuan He[1], Jean-Claude Sibuet[2], Longtao Sun[1], Xuelin Qiu[1], Pingchuan Tan[3], and Jian Wang[4]

[1]Key Laboratory of Ocean and Marginal Sea Geology, South China Sea Institute of Oceanology, Chinese Academy of Sciences, Guangzhou, China, [2]Ifremer Centre de Brest, Plouzané, 44 rue du Cloitre, France, [3]Center for Earth Evolution and Dynamics, University of Oslo, Oslo, Norway, [4]Department of Ocean Science and Engineering, South University of Science and Technology of China, Shenzhen, China

Key Points:
- 6–10 Myr postspreading volcanism occurred several Myr after spreading ceased in the South China Sea
- Postspreading volcanism was located inside an 80 km wide zone of thin oceanic crust (<5 km), oblique to the N055° extinct spreading ridge
- The buoyancy-driven partial melting model might explain the influence of the Hainan plume on postspreading volcanism

Correspondence to:
M. Zhao,
mhzhao@scsio.ac.cn;
E. He,
eyhe@scsio.ac.cn

Citation:
Zhao, M., He, E., Sibuet, J.-C., Sun, L., Qiu, X., Tan, P., et al. (2018). Postseafloor spreading volcanism in the central east South China Sea and its formation through an extremely thin oceanic crust. *Geochemistry, Geophysics, Geosystems*, *19*, 621–641. https://doi.org/10.1002/2017GC007034

Received 24 MAY 2017
Accepted 5 FEB 2018
Accepted article online 9 FEB 2018
Published online 8 MAR 2018

Abstract *P* wave velocity models were obtained by forward and inverse modeling from 38 ocean bottom seismometers deployed in the central East subbasin of the South China Sea (SCS). Four types of crust have been defined: (a) thin oceanic crust (<5 km), (b) typical oceanic crust (5–6 km), (c) thick oceanic crust hosting postspreading volcanoes (>6 km) with significant intrusive roots, and (d) thick oceanic crust with enhanced spreading features (>6 km) but without significant roots. Within the central East subbasin, the thin oceanic crust, only identified inside an 80 km wide zone, is located within an overall 150 km wide domain characterized by N055° seafloor spreading trends. The postspreading volcanoes were formed during a N-S tensional episode around 6–10 Ma, several millions of years after seafloor spreading ceased in the SCS. Seafloor spreading (N055° and N145°) and postspreading (N000° and N090°) features are observed in the morphology of some of these volcanoes. The rupture of the brittle thin oceanic crust was focused where the crust was the weakest, i.e., at the intersection of the extinct spreading ridge with former fracture zones. From geological and geophysical arguments, we suggest that the postspreading volcanism might have been influenced by the Hainan plume activity through a buoyancy-driven partial melting mechanism.

1. Introduction

The South China Sea (SCS) is a marginal sea located at the confluence of the Eurasian, Philippine Sea, and Indian-Australian plates. Rifting in this region occurred during early Tertiary times (e.g., Franke et al., 2014) and ended at ~33 Ma, as shown at IODP Site U1435 location (Figure 1) where a sharp unconformity is revealed between deep marine facies above sandy lithologies of shallow marine deltaic and coastal facies (Expedition 349 Scientists, 2014). The oldest seafloor spreading magnetic lineation identified in the SCS is C12 (32 Ma; Barckhausen et al., 2014; Briais et al., 1993) and was formed right after the end of the rifting phase. However, the end of seafloor spreading in the SCS is not firmly established. Different models for the oldest seafloor spreading include either at ~15.5 Ma as suggested by Briais et al. (1993) and Li et al. (2014) or at 20.5 Ma by Barckhausen et al. (2014). At a more global scale, kinematic reconstructions (e.g., Hall, 2002; Sun, 2016) show the extreme complexity of the formation of the South China marginal sea, which was recently exacerbated by the Wu et al. (2016) kinematic modeling using the positions and lengths of subducted slabs in their reconstruction methods. The large differences between these two types of global kinematic reconstructions explain why numerous papers dealing with the SCS placed within conventional geological and local kinematic frameworks generally lead to erroneous conclusions. In such a complex geodynamic environment, we should test SCS kinematic models (e.g., Barckhausen et al., 2014; Briais et al., 1993; Li et al., 2014) as well as structural and tectonic models with a critical approach based on the use of high-quality geophysical, geochemical, and geochronological data sets. Such an approach is pertinent in particular to explain the large volume of SCS postspreading volcanism predominantly observed in the axial parts of the East and SW subbasins (more than 90% of its total volume), mostly in the vicinity of the Zhongnan faults zone, a major feature, which separates these two subbasins (Figure 1). There, the last phase of seafloor spreading is N055° oriented in a ~150 km wide strip (Sibuet et al., 2016) and the postspreading Zhenbei-Huangyan seamount chain is oriented E-W over a distance of 220 km within this strip. It contradicts

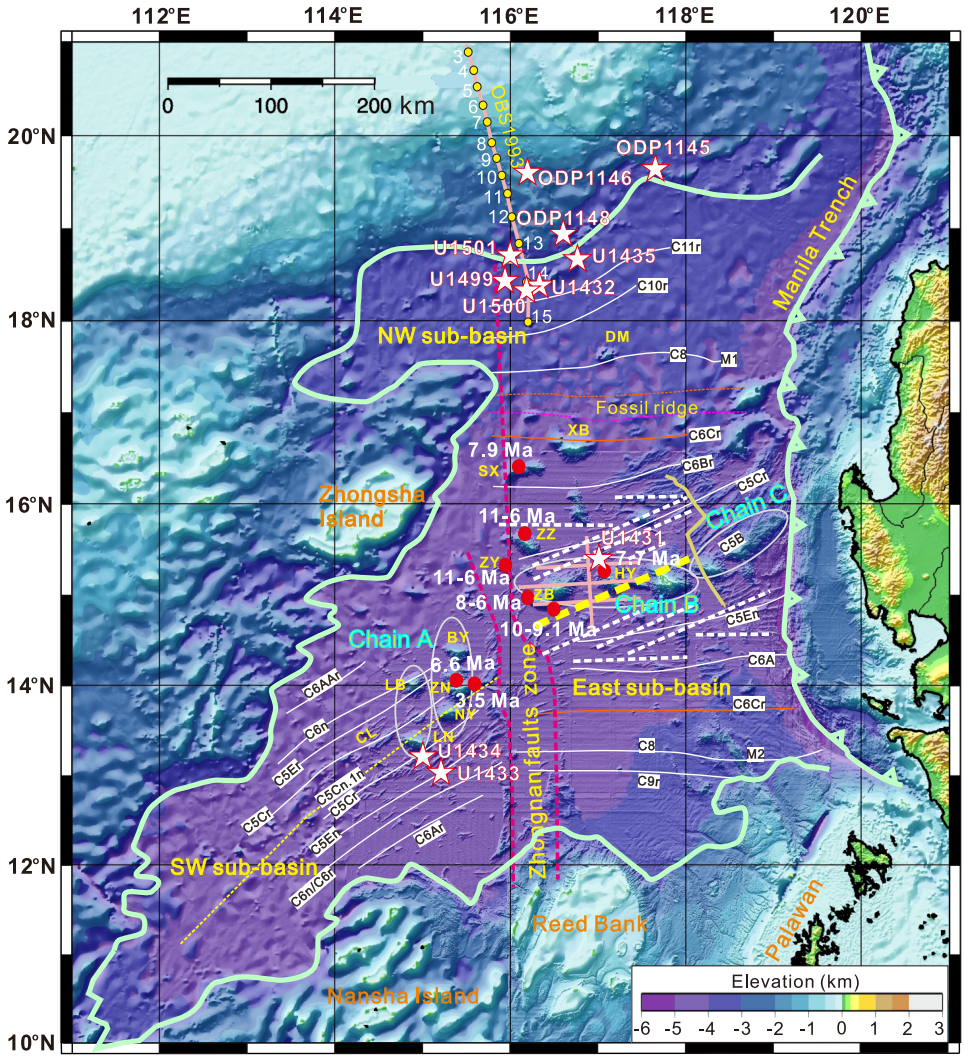

Figure 1. Swath-bathymetric map of the South China Sea (SCS; Barckhausen et al., 2014) and postspreading volcanism. OBS seismic survey lines in light pink are located in the axial region of the East subbasin (Zhenbei and Huangyan seamounts chain) and on the northeastern margin. The solid cyan line represents the continent-oceanic boundary and the solid cyan line with triangles the Manila trench (Sibuet et al., 2016). The white stars are location of ODP and IODP Sites (ODP Sites 1145, 1146, and 1148 and IODP Sites U1431 to U1435 (Expedition 349 Scientists, 2014) and U1499 to U1501 (IODP legs 367 and 368)). Seamount names in yellow color, dredge samples correspond to red dots with ages labeled in white: DM, Daimao; XB, Xianbei; SX, Shixing, 7.9 Ma (Yan et al., 2008b); ZZ, Zhangzhong, 11–6 Ma (Pautot et al., 1990); ZY, Zhiyou, 11–6 Ma (Pautot et al., 1990); ZB, Zhenbei, 8–6 Ma (Pautot et al., 1990) and 10–9.1 Ma (Tu et al., 1992; Wang et al., 1984); HY, Huangyan, 7.7 Ma (Wang et al., 2009); BY, Beiyue; ZN, Zhongnan, 6.6 Ma (Yan et al., 2014) and 3.5 Ma (Tu et al., 1992); NY, Nanyue; LB, Longbei; LN, Longnan; CL, Changlong. The four ovals indicate the two N-S trending Chain A, E-W trending Chain B, and NE-SW trending Chain C. The thick dashed yellow lines represent the extinct spreading ridge (ESR), and N055° trending white dashed lines magnetic lineations identified in this study. For comparison, thin white solid lines are magnetic lineations identified by Li et al. (2015b). M1 and M2 are two characteristic magnetic lineations (Li & Song, 2012) identified as C8 and dated ~27.5 Ma (Briais et al., 1993) or 26 Ma (Gradstein et al., 2005). The location of the Zhongnan faults zone (red dashed lines) is from Li et al. (2015b). East of the yellow broken line located between Chains B and C, magnetic lineations cannot be defined because of the presence of transfer faults, pseudo-faults and overlapping spreading centers (Hsu et al., 2016).

what was previously published with the last phase of spreading oriented E-W and parallel to the postspreading chain of volcanoes (e.g., Barckhausen et al., 2014; Briais et al., 1993; Li et al., 2015a, 2015b). Thus, a new relocalization of the trends of magnetic lineations and their identifications are still required.

The objective of this paper is to understand the nature, age, and mode of emplacement of the voluminous postspreading volcanism, with emphasis on the following questions: How and when was postspreading volcanism

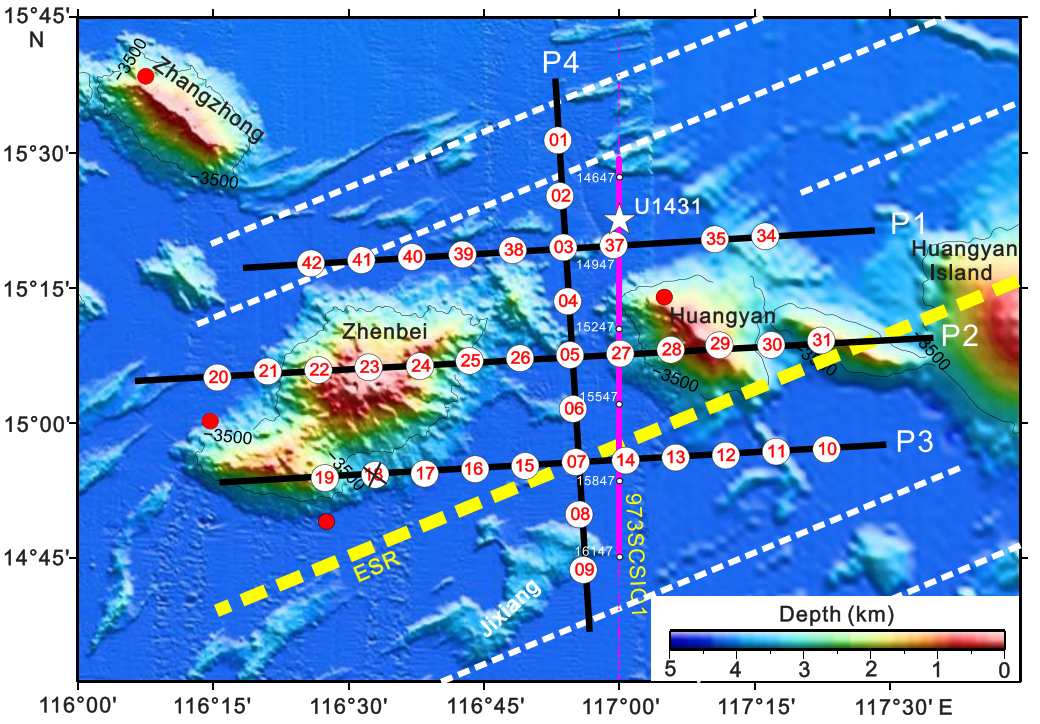

Figure 2. Detailed swath-bathymetric map of the Zhenbei and Huangyan seamounts chain with the location of the four wide-angle reflection/refraction lines. The thick black lines represent OBS Profiles P1, P2, P3, and P4 and the white circles with red labels the location of OBSs. OBS18 did not record useful data. Red dots are the locations of dredged samples (Pautot et al., 1990; Tu et al., 1992; Wang et al., 1984, 2009) and the white star is the location of IODP Site U1431 (Expedition 349 Scientists, 2014). The purple line is MCS profile 973SCSIO1 shown in Figure 9 and white circles are shot numbers. The extinct spreading ridge (ESR) shown by a thick yellow dashed line and N055° trending magnetic lineations shown by white dashed lines are from this study.

emplaced? Can we quantify the amount of excess volcanism along the Zhenbei-Huangyan seamounts chain? Where was the East subbasin extinct spreading ridge (ESR) located at the end of the spreading phase?

To answer the above questions, we carried out a high-precision, crustal-scale, wide-angle seismic survey (Figures 1 and 2), which covered the E-W trending Zhenbei-Huangyan seamounts chain (Zhang et al., 2013), and consists of three E-W oriented profiles (P1, P2, and P3) cut across by a N-S profile (P4). Single-channel seismic profiles were also collected during the survey. We interpret the velocity structures established by forward and inverse modeling along these four profiles in the framework of available Bouguer gravity and magnetic anomaly data, detailed swath-bathymetry and multichannel seismic reflection (MCS) data.

2. Geological Setting of the Postspreading Volcanism in the Central Part of the South China Sea

Postspreading volcanic seamounts are numerous and voluminous in the central parts of the East and SW subbasins. They are rare north of the central part of the East subbasin and almost absent south of it (Figure 1). These seamounts, formed after the formation of the SCS oceanic crust, are different in their morphology and geochemical composition from seamounts created at the ridge axis during the formation of the oceanic crust of the SCS. Three seamount chains are identified. These include (1) two N-S trending seamounts chains (Longbei and Longnan seamounts; Nanyue, Zhongnan, and Beiyue seamounts) located between 114.8°E and 115.6°E longitude in the SW subbasin (Chain A); (2) an E-W trending chain of seamounts (Chain B) where the largest seamounts are aligned immediately east of the Zhongnan faults zone. Chain B, named the Zhenbei-Huangyan seamounts chain in its western part, consists of five major seamounts, which stand nearly 4,000 m above the seafloor (Yao, 1996) and is oriented obliquely to the surrounding N055° seafloor spreading trends. (3) Further east, Chain C is approximately parallel to the N055° recent seafloor spreading trends. Chain C is located east of an irregular continuous broken yellow line

approximately located at ~118°E longitude (Figure 1). We will not discuss Chain C because of its complexity due to the presence of overlapping spreading centers, transfer faults and pseudo-faults related to the change of direction of spreading centers east of this boundary (Hsu et al., 2016).

The two parallel N-S trending alignments of seamounts (Chain A) as well as several N-S trending features identified in detailed swath-bathymetric maps (Sibuet et al., 2016, Figure 8a) suggest that these N-S trends are fracture zones (FZs) that belong to the postspreading phase of extension. These N-S FZs are present inside the ~150 km wide corridor (Figure 1) where N055° spreading lineaments were identified (Sibuet et al., 2016). Outside this ~150 km wide strip, spreading lineaments are more or less ~E-W oriented and FZs are mostly ~N-S oriented, precluding unambiguous determination of a N-S postspreading phase of extension. Thus, on each side of the Zhongnan fault zone (Figure 1), the postspreading volcanic seamount chains were emplaced along N-S and E-W directions as if these trends were corresponding to FZs and spreading directions of a N-S phase of extension. The amount of extension during the postspreading phase is unknown but might be on the order of a few kilometers (Sibuet et al., 2016).

3. Single-Channel Reflection and Wide-Angle Seismic Refraction Data

3.1. Data Processing

We first processed the 18 single-channel reflection profiles collected during ocean bottom seismometers (OBS) recordings. Using stratigraphic correlations between the MCS Profile 973SCSIO1 (Figure 2) and coring/logging data from IODP Site U1431, Figure 3 shows seismic sequence boundaries along the four single-channel seismic profiles coincident with the OBS profiles. *Tmm*, *Tmp*, and *Tpp* are middle Miocene/late Miocene (~11.1 Ma), Miocene/Pliocene (~5.2 Ma), and Pliocene/Pleistocene (~2.6 Ma) boundaries, respectively (Li et al., 2015a). Velocities and thicknesses of sediments were determined by using the quadratic time-depth conversion function $z = 0.000188295t^2 + 0.695896t$, where z is the depth in meters below the seafloor and t is the two-way travel time (TWTT) in ms (Li et al., 2015a).

The 41 OBS data processing includes instrument relocation and band-pass filtering (3–12 Hz; Zhang et al., 2013). As examples of OBS recordings, picking phases, PmP phases, ray tracing, and travel times simulation are published for Profile P4 in He et al. (2016); other examples will not be displayed in this paper. *P* wave velocity models along these four profiles were first derived by forward modeling using the *Rayinvr* code of Zelt and Smith (1992). The initial model includes seafloor and basement interfaces computed in depth from the coincident single-channel seismic profiles (Figure 3). The forward model parameters are shown in Table 1. Velocities are assumed to be laterally homogeneous. The velocity models were continuously adjusted to fit the observed and theoretical travel times by using the trial and error method of Zelt and Smith (1992). The travel time uncertainties are estimated to be 50, 70, and 90 ms for Pg, PmP, and Pn arrivals, respectively, depending on the quality of travel time picks for Profiles P1, P3, and P4. For Profile P2, the travel time uncertainties are larger than for other profiles (70, 90, and 110 ms for Pg, PmP, and Pn arrivals, respectively) because the topography changes more significantly along the profile.

The four *P* wave velocity models were also determined by using the *Tomo2d* joint refraction and wide-angle reflection travel time inversion (Korenaga et al., 2000). This tomographic approach requires much less a priori information and tends to prevent overinterpretation of data. Data fitting is also quantified using χ^2 values (Table 1), the mean square of residuals normalized by the picking uncertainty. The final models correspond to travel time residuals of less than 1 s and normalized χ^2 values ideally close to 1. The Moho interface is freely updated as a floating reflector during modeling. To secure the accuracy of processing and better discuss the results of modeling, forward models were homogenized in order to minimize the differences between forward and tomographic models. Data quality and seismic ray coverage of the wide-angle data are good for the four profiles (Figure 4 and Table 1). Finally, the reliabilities were assessed by density of ray paths and resolvability through checkboard tests (Figure 5) for the four profiles.

3.2. Accuracy and Resolution Tests

The derivative weight sum (DWS) is the column-sum vector of the velocity kernel. It measures the ray coverage, which estimates ray density with a hit count that weights each ray by its distance to the model parameter (Korenaga et al., 2000). The DWS of the final velocity models is shown for each of the four profiles (Figure 5). White areas correspond to poorly constrained regions (DWS < 1.0). However, the DWS does not

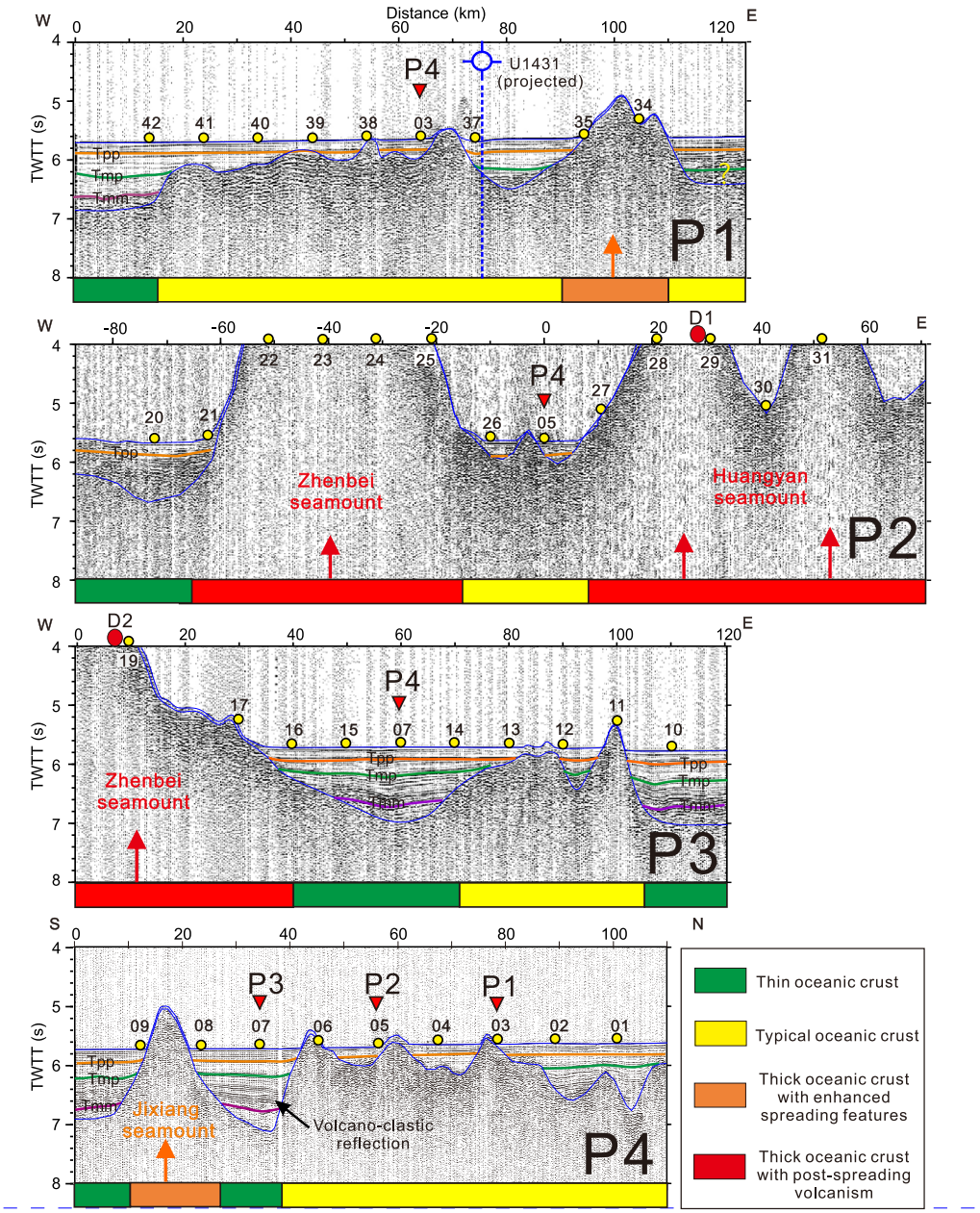

Figure 3. Single-channel seismic Profiles P1, P2, P3, and P4 located in Figure 2. TWTT, two-way traveltime in seconds. The basement is underlined by thin blue lines. Purple, green, and orange lines are seismic sequence boundaries dated middle Miocene/late Miocene (*Tmm*), late Miocene/Pliocene (*Tmp*), and Pliocene/Pleistocene (*Tpp*; Li et al., 2015a). Volcano-clastic sediments result from erosion of the adjacent seamount formed during the postspreading phase of extension. Yellow circles, OBSs locations. Red inverted triangles are intersections between the four profiles. IODP Site U1431 (blue circle) is projected in the N145° direction on Profile 1. Red dots (D1 and D2 on P2 and P3 profiles, respectively) are locations of projected dredged samples in the N145° direction (Pautot et al., 1990; Tu et al., 1992; Wang et al., 1984, 2009). The underlying bars represent thin oceanic crust (green), typical oceanic crust (yellow), thick crust with enhanced spreading features (orange), and thick crust with postspreading volcanism (red) based on MCS and refraction data. Orange and red vertical arrows indicate enhanced spreading features and postspreading volcanism, respectively.

provide any quantitative information about the resolution of the model. Checkerboard tests are commonly used for model assessment and resolution analysis using synthetic data. This kind of tests aims to examine the ability to recover the velocity anomaly pattern superimposed on the velocity model (Zelt, 1999). A perturbed velocity model was created from the starting model with 5% alternate positive and negative

Table 1
Forward and Inversion Model Parameters

Profile	Number of OBSs	Number of picks		Nodes	Dimensions		Grid spacing (km)	
		Refraction	Reflection		*X*	*Z*	*X*	*Z*
Forward model parameters								
P1	9	2,026	413	64,113	497	129	0.25	0.125
P2	13	4,412	748	105,777	657	161	0.25	0.125
P3	10	1,894	276	62,049	481	129	0.25	0.125
P4	9	2,252	251	56,889	441	129	0.25	0.125

Profile	Number of iterations	Smoothing (%)		Dampling (%)		Correlation length (km)		χ^2		RMS (ms)	
		Veloc.	Depth	Veloc.	Depth	Horiz.	Vertical	Initial	Final	Initial	Final
Inversion model parameters											
P1	10	45	5	10	10	2–4	0.2–2	82.64	1.67	666	78
P2	6	120	5	10	10	2–4	0.2–2	94.45	1.71	699	105
P3	10	45	5	10	10	2–4	0.2–2	53.92	1.23	584	74
P4	10	45	5	10	10	2–4	0.2–2	80.24	1.63	512	80

anomalies. The patterns in the sinusoidal functions are characterized by half-wavelengths of 10 and 3.5 km in the horizontal and vertical directions, respectively (Figure 5). Synthetic travel times, with the same source-receiver configuration used in our model, were calculated by adding a Gaussian random noise with a standard deviation of 10 ms. Then, the recovered models were computed by inversion of the perturbed velocity model using the same inversion parameters and synthetic data. A large range of checkerboard patterns were tested and three representative examples of resolved checkerboard patterns are shown for each of the four profiles (Figure 5). Cells with a size of 8 km horizontally and 3.5 km vertically are the threshold for P1, P3, and P4 models and cells with a size of 10 km horizontally and 3.5 km vertically are the threshold for the P2 model. Velocity models present an optimal resolution in their central parts and a good recovery of velocity perturbations with a large ray density coverage in the upper panels of Figure 5. These tests show that the inversion cannot constrain velocity variations at depths greater than 14 km below the seafloor for the four profiles (Figure 6) and that the size of cells constrains the geophysical interpretation to features not smaller than 8 km × 3.5 km for P1, P3, and P4 and 10 km × 3.5 km for P2.

3.3. Interpretation of the Four Wide-Angle Seismic Reflection and Refraction Profiles

In general, the oceanic crust consists of two layers: a low velocity upper crust (3.0–6.4 km/s) and a high-velocity, low-gradient lower crust (>6.4 km/s; e.g., Minshull & White, 1996; Muller et al., 1997; White et al., 1992). The 6.4 km/s velocity contour generally coincides with the boundary between layers 2 and 3 (Harding et al., 1993). For all our profiles, the velocity structures computed with forward (*Rayinvr*) and tomographic (*Tomo2d*) modelings (Figure 4) are similar. These good fits suggest that our crustal models contain minimal uncertainties. As there are no layer interfaces in tomographic models, forward modelings are used to discuss the nature of the crust, the crustal thickness of layers 2 and 3 as well as the depth of interfaces (Figure 6). 1-D velocity-depth profiles extracted from *Rayinvr* and *Tomo2d* models beneath all OBSs stations in the four profiles appear in Figure 7. They display interfaces (such as 6.4 or 7.0 km/s iso-contours) and velocity gradients for the forward modeling that are complementary with the velocity values and gradients derived from the tomographic inversion modeling. Based on sediment distribution and our crustal modeling, four different types of crust are defined: thin oceanic crust (<5 km), typical oceanic crust (5–6 km), thick oceanic crust hosting postspreading volcanoes (>6 km) with significant intrusive roots, and thick oceanic crust with enhanced spreading features (>6 km) but without significant roots under the postspreading volcanic seamounts, that in Figures 3 and 7 are depicted as green, yellow, orange, and red areas, respectively.

Profile P1 is located north of the Zhenbei-Huangyan seamounts and runs closest to IODP Site U1431 (Figure 2). The crustal thickness is between 4.8 and 6.3 km with similar thicknesses for layers 2 and 3 (Figures 4 and 6). The crustal structure is dominated by a typical oceanic crust (yellow portion of color bar in Figure 3), similar to

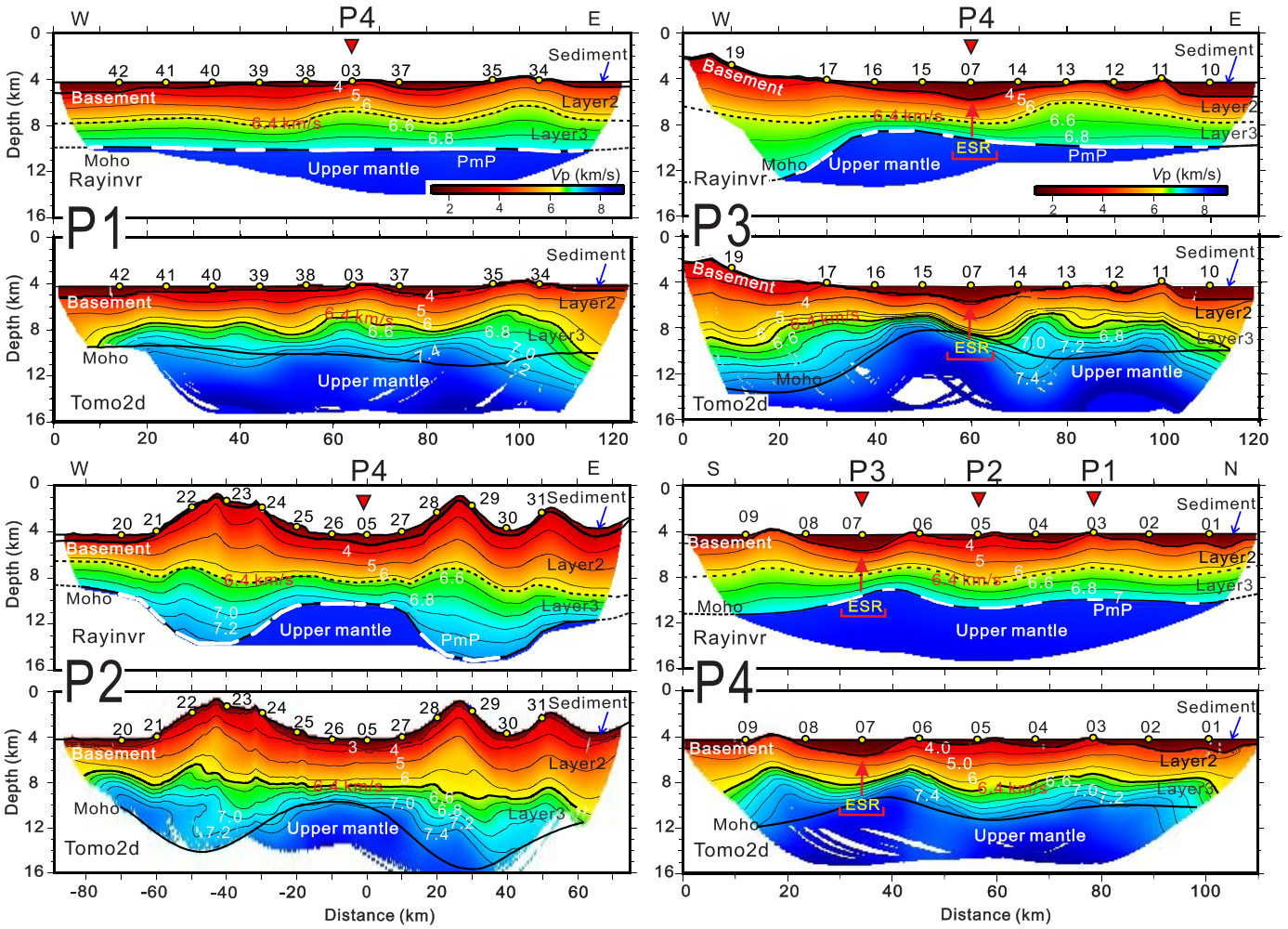

Figure 4. *P* wave crustal structures of the four seismic profiles with same color velocity bar for all profiles. Yellow circles are OBSs locations. ESR, extinct spreading ridge. The red inverted triangles are intersections between the four profiles. Distances (in km) correspond to distances on seismic reflection profiles (Figure 3). For each profile, the upper structure is obtained with the *Rayinvr* software (Zelt & Smith, 1992). Black lines and dashed black lines represent the basement and the 6.4 km/s velocity contour, respectively. The thick white segments overlying solid black lines indicate where the Moho interface is constrained by PmP arrivals. Layer 2/layer 3 and Moho interfaces are extrapolated at the extremities of each profile (dashed lines). The lower structures are obtained with the *Tomo2d* code (Korenaga et al., 2000). The thick black lines represent the basement, the 6.4 km/s velocity contour and the Moho interface obtained by inversion. The 6.4 km/s iso-velocity contour is the layer 2/layer 3 interface generally associated with the sharpest change in velocity gradient (Minshull & White, 1996; Muller et al., 1997).

a crust formed at a slow spreading rate (White et al., 1992), except for the OBS42 that is located at the western end of the profile (0–17 km) where the oceanic crust is thin (green portion of color bar) and characterized by a deep basement and a thick layer of sediments (1.2 s TWTT in Figure 3). There, the reflection sequence boundary *Tmm* (∼11.1 Ma) has been identified in the MCS profiles for IODP Site U1431 (Li et al., 2015a). The velocity structure observed (green portion of color bar in Figure 3) points to a 4.8 km thin oceanic crust and a basement at a depth of 5.2 km (6.8 s; Figures 3, 4 and 6) seem not to have been affected by postspreading magmatic processes. From OBS35 to the east of OBS34 (95–113 km, orange portion of color bar in Figures 3 and 7), the observed velocity structure is typical of oceanic crust (6.3 km in thickness) with topographically enhanced spreading features (Figure 3). In this part, the profile corresponds to an obvious abyssal hill fabric on the swath-bathymetric map (Figure 2), but the underlying Moho is not deflected as confirmed by high Bouguer anomalies (Figures 8a and 8b) and the crust is not affected by postspreading magmatic processes (Figures 6 and 7a).

Profile P3 cuts across the southern part of the Zhenbei-Huangyan postspreading volcanic features in its western extremity (0–40 km). Even if the velocity structure is not well constrained there (Figure 4), the underlying Moho is clearly deflected, with a thick crust associated with the emplacement of the postspreading Zhenbei seamount (Figures 3, 4, 7, and 8). OBS19 shows velocities lower than those of the oceanic

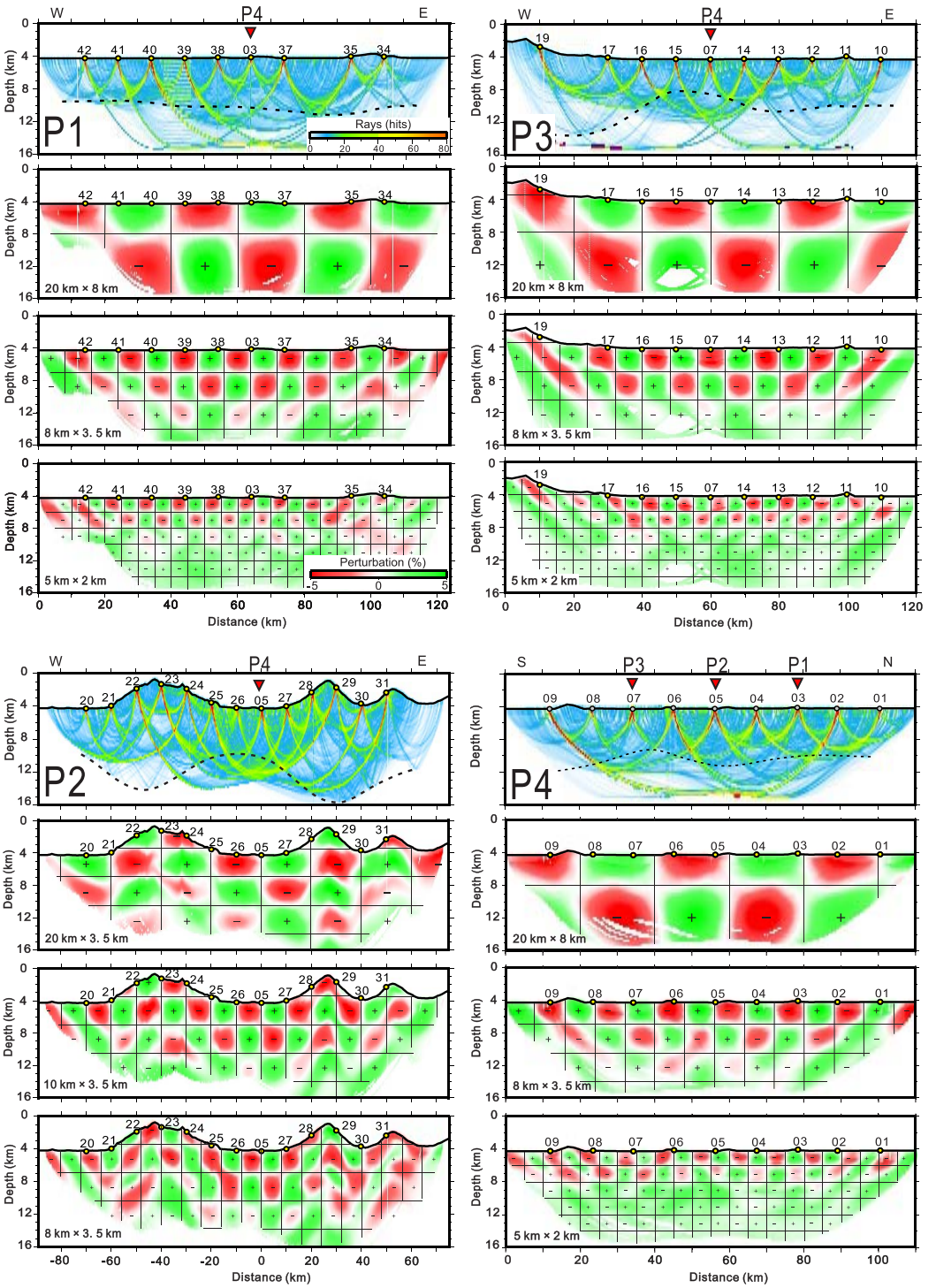

Figure 5. (top) Derivative weight sum and (bottom three) recovered checkerboard tests for the four profiles. Dashed lines are Moho interfaces. Checkerboard tests after inversion with velocity perturbation anomalies of 5% (positive in green and negative in red). The three checkerboard panels show resolved checkerboard patterns with different cells for each profile. The threshold checkerboard cells are 10 km × 3.5 km for the P2 profile and 8 km × 3.5 km for the other three profiles. Other symbols as in Figure 4.

bounds of White et al. (1992) down to a depth of at least 9 km (Figure 7c2), which clearly characterizes the postspreading volcanic thick crust (in red; Figures 3, 4, and 8c). Outside the Zhenbei seamount (east of OBS16), the crustal thickness is between 3.5 and 6 km with a mean thickness of layers 2 and 3

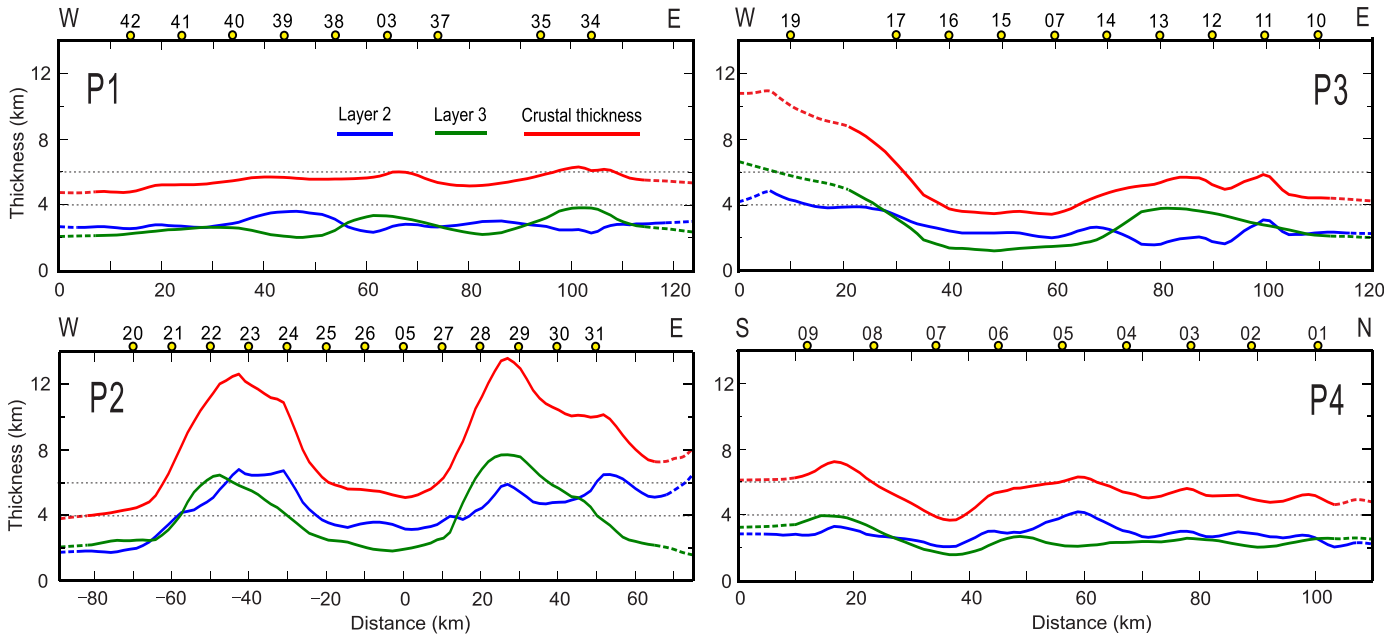

Figure 6. Variations of crustal (red), oceanic layer 2 (blue), and oceanic layer 3 (green) thicknesses along the four profiles based on the *Rayinvr* models of Figure 4. Dashed portions of lines at the end of each profile are extrapolated as in Figure 4, where the layer 2/layer 3 and Moho interfaces are extrapolated at their extremities.

approximately identical (Figures 4 and 6), even if local variations of layers 2 and 3 thicknesses are much greater than for Profile P1. Between OBS16 and OBS14 (40–70 km) as well as east of OBS11 (103–120 km), the crust is very thin, between 3.5 and 4.5 km (green color, thin oceanic crust; Figures 3, 4, 6, and 7c), with velocities corresponding to upper mantle velocities (>8.0 km/s) at depths larger than 4 km below the basement (OBS15 and OBS7 in Figure 7c2). The basement depth here reaches 5.8 km (7.0 s) compared with 5.2 km (6.8 s) at OBS42 for Profile P1 (Figures 3 and 4). In both Profiles P1 and P3, the *Tmm* (~11.1 Ma) reflection sequence boundary is identified (Figure 3). The turbiditic sedimentation (Li et al., 2015a), characterized by onlaps on the oceanic basement, seems to widely occur as soon as the oceanic crust is created. In Profile P3, about 0.5 s of layered sediments were deposited before the *Tmm* sequence boundary. It means that turbiditic sediments were probably deposited close to the ESR since the end of SCS opening, or just after, on the thin oceanic crust. From OBS14 to just west of OBS11 (70–103 km), the thickness of the crust is between 5 and 6 km (yellow, typical oceanic crust) as for most of Profile P1. For the typical oceanic crust, the turbiditic deposition occurs much later, somewhere in between the *Tmp* (~5.2 Ma) and the *Tpp* (~2.6 Ma; Li et al., 2015a) sequence boundaries. The major difference between typical and thin oceanic crusts (yellow *versus* green portions in Figure 3) is that the mean basement depths for the two types of typical and thin oceanic crusts are at ~6.0 s versus ~7.0 s, respectively (Figure 3), explaining why the early turbiditic sedimentation was absent on the oceanic crust formed at shallower depth.

Profile P2 cuts across the Zhenbei-Huangyan seamounts chain where topographic variations are the largest (Figure 2). The crustal structure of Profile P2 mostly shows an abnormally thick crust compared to typical oceanic crust (Figures 4, 7b1, 7b2, 8a, and 8b). The crustal thicknesses beneath the Zhenbei (OBS23) and Huangyan (OBS29) seamounts are up to 12.0 and 13.2 km (Figures 6, 7b1, and 7b2), respectively. All OBSs with velocities lower than those of typical oceanic crust and with crustal thicknesses larger than 6 km (Figure 6) belong to the thick postspreading volcanic crust (red color; Figure 3). The crust below OBS20, located at the western end of Profile P2, displays characteristics of thin oceanic crust (green color, Figures 3 and 7b), a basement depth at 4.8 km (~6.8 s) and a crustal thickness of ~4.0 km (Figures 3, 4, 6, and 7), as for Profile P1. The crust beneath OBS26 and OBS05, located in between the two seamounts, with a thickness of 5–6 km, is typical oceanic crust (yellow color, Figures 6 and 7). Figure 4 shows that the 6.4 km/s interface is approximately horizontal below the Zhenbei and Huangyan seamounts. The upper part of layer 2, characterized by low velocities, is possibly composed of highly porous volcanic clastic material or pillow lavas, which is consistent with the lithology of dredged samples (Wang et al., 2009). Concerning layer 3, the 7.0–7.4 km/s high-velocity layer located at the base of the crust below the two seamounts does not exist elsewhere.

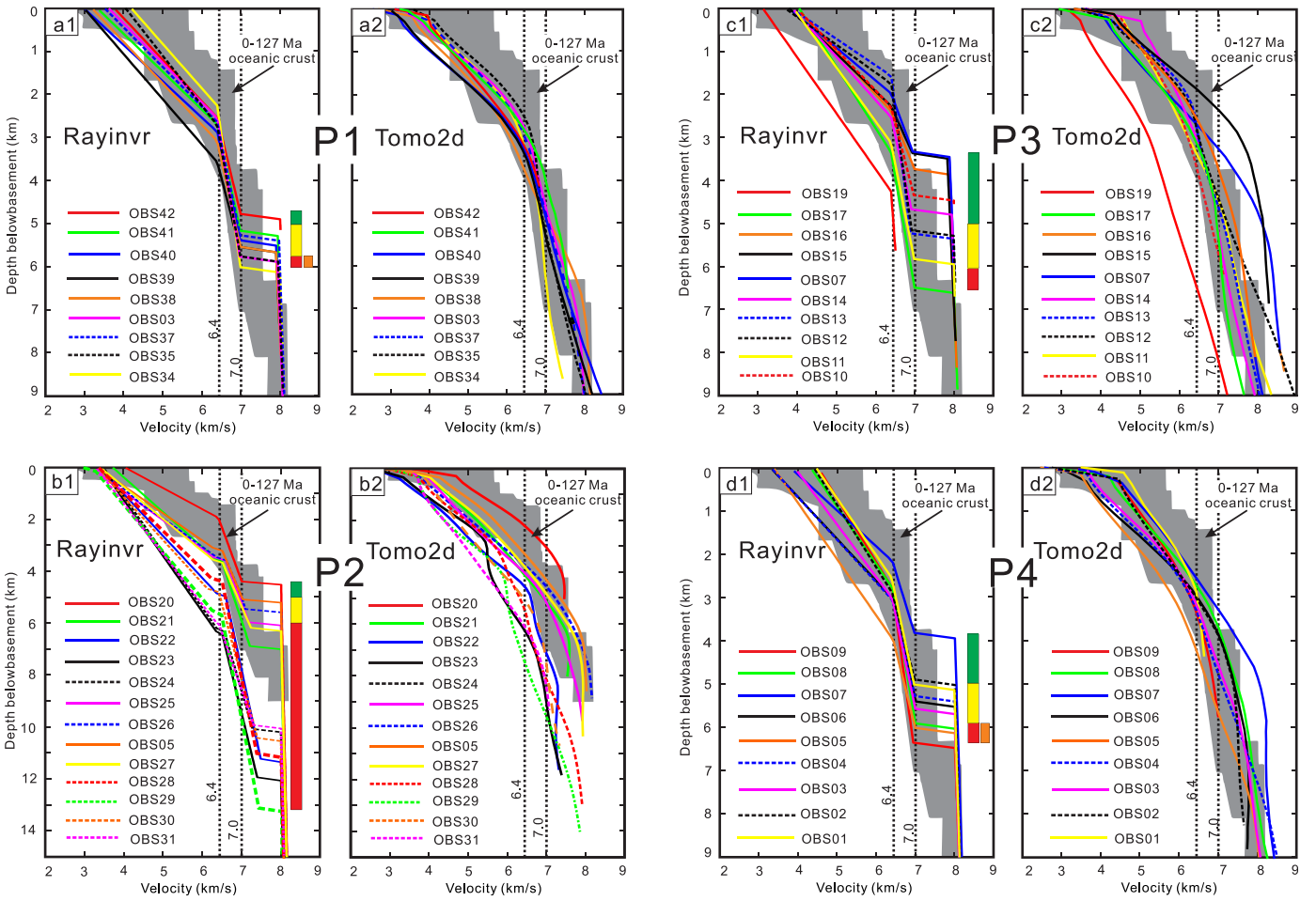

Figure 7. 1-D velocity-depth profiles beneath all OBSs extracted from the four velocity profiles obtained with *Rayinvr* and *Tomo2d* softwares (location of OBSs in Figures 2 and 4). For comparison, OBS03 at the intersection of P1 and P4, OBS05 at the intersection of P2 and P4, and OBS07 at the intersection of P3 and P4 are displayed with the same types of lines and colors. Grey-shaded area is the 0–127 Ma velocity range for the Atlantic oceanic crust (White et al., 1992). As in Figure 3, the green, yellow, red, and orange bars in *Rayinvr* models indicate thin oceanic crust, normal oceanic crust, postspreading volcanic thick crust, and oceanic crust with enhanced spreading features, respectively.

Profile P4, where topographic changes are minimal, is perpendicular to the Zhenbei-Huangyan seamounts chain (Figure 2) and located in between the two seamounts. The crustal thickness varies between 3.7 and 7.2 km (Figures 4 and 7d). The velocity structure from OBS01 to OBS06 (38–110 km) shows that the crust is typical oceanic crust (yellow color), which has not been affected by postmagmatic processes. From 38 km (nearly beneath OBS07, Figure 3) to the southern extremity (0 km), the crust is thin oceanic crust (green color) except for the Jixiang seamount (10–30 km) where the crust (5.8–7.3 km thickness) is oceanic crust with enhanced spreading features (orange color; Figures 3, 4, 6, and 7d) and is characterized by high Bouguer anomalies (Figure 8b). Thus, the crust beneath OBS07 is extremely thin (3.7 km), with basement at a depth of 5.8 km (7.1 s), both along Profiles P3 and P4. Below OBS07, *Tomo2d* models confirm these results and that mantle velocities are reached at a depth of 3.7 km below basement (Figures 7c2 and 7d2).

4. Analysis and Discussion

4.1. Nature of the Crust in the Axial Part of the East Subbasin Before the Postseafloor Spreading Volcanic Phase

The thin oceanic crust (~3.7 km) near OBS07 in Profiles P3 and P4, is also observed beneath OBS42 in Profile P1, OBS20 in Profile P2, and OBS10 in Profile P3 (Figures 3, 4, 7, and 8). At all these locations, the thin oceanic crust corresponds to negative free-air gravity anomalies (Figure 8a), and moderate values (270–290 mGal) of Bouguer anomalies (Figure 8b). The thin oceanic crust (green in Figure 3) shows fairly robust

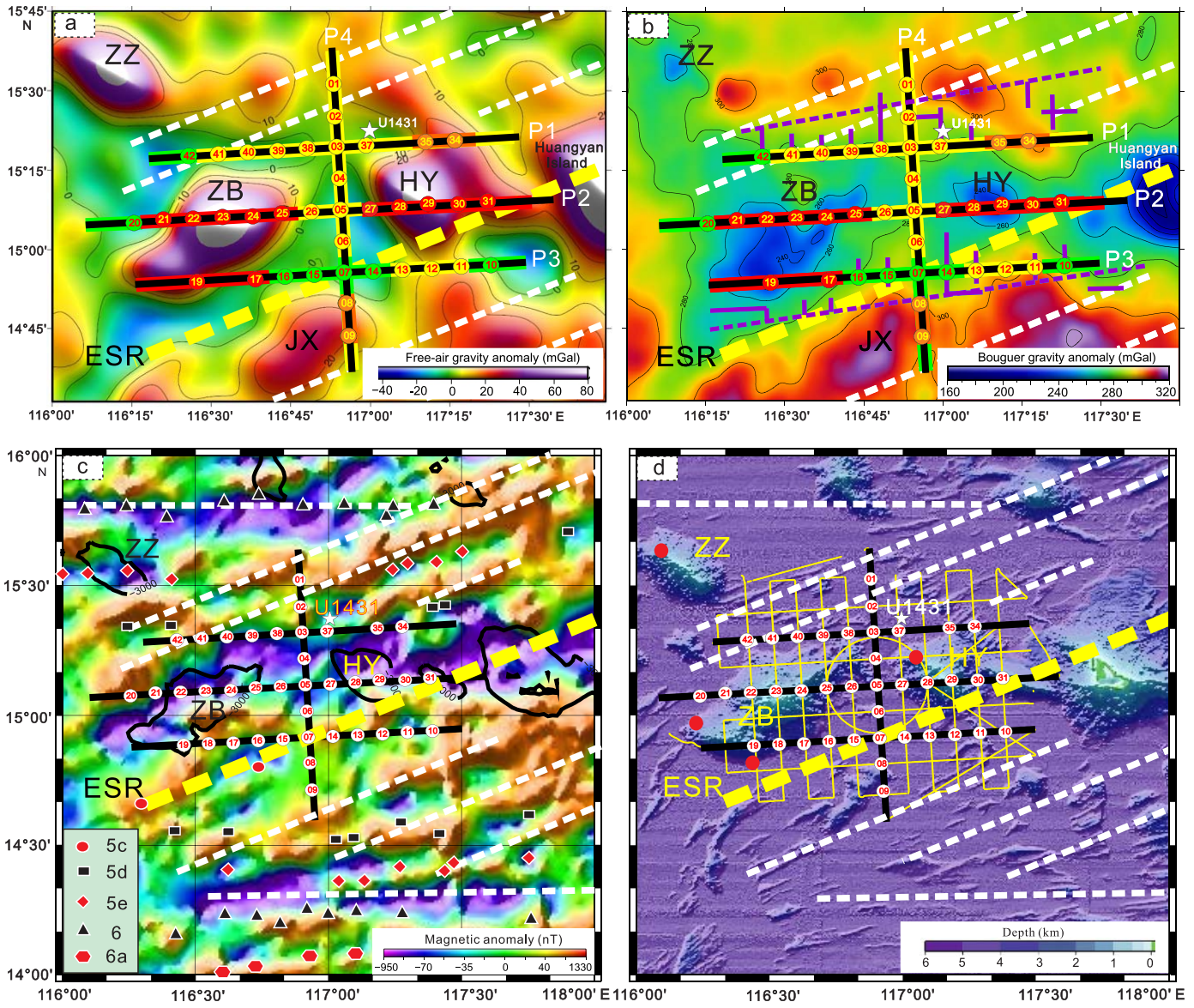

Figure 8. The four types of crust (typical oceanic crust in yellow, thin oceanic crust in green, postspreading volcanic thick crust in red, and oceanic crust with enhanced spreading features in orange) are displayed along refraction lines. The white dashed lines and the yellow dashed line are our final magnetic lineations pattern and the location of the extinct spreading ridge (ESR) identified in Figure 8c and shown in the other panels. ZZ, ZB, and HY are Zhangzhong, Zhenbei, and Huangyan seamounts, respectively. Other legends are the same as in Figure 2. (a) Free-air gravity anomaly map (Sandwell et al., 2014) and (b) Bouguer gravity anomaly map computed from Sandwell et al. (2014). Purple continuous lines underline where the sediment thickness exceed 1.2 s TWTT on the 18 single-channel profiles with their envelope shown by purple dashed lines. (c) Magnetic anomalies of the Zhenbei and Huangyan seamounts chain (Ishihara & Kisimoto, 1996) with Li et al. (2015b) interpretation (black and red symbols for magnetic chrons C5c, C5d, C5e, C6, and C6a) and our interpretation (dashed white lines and ESR yellow dashed line) based on magnetic, swath-bathymetric, gravity, reflection and refraction data. (d) Swath-bathymetry map with the location of the four OBS profiles (thick black lines), the shooting lines (thin yellow continuous lines) and our final interpretation.

features as a deep basement and clear *Tpp* (~2.6 Ma), *Tmp* (~5.2 Ma), and *Tmm* (~11.1 Ma) stratigraphic sequences boundaries (Li et al., 2015a). The presence of the thin oceanic crust may be related to magma deficient activity at the end of the formation of oceanic crust in the central part of the East subbasin. A similar type of crust is found along the extinct Aegir Ridge in the NE Atlantic Ocean, where the crustal thickness is as thin as 4.5 km due to magma poor activity (Breivik et al., 2006), suggesting some temporal evolution of the asthenospheric temperature and/or composition at least at the end of the SCS opening. The SCS spreading ridge extinction during early to middle Miocene is probably related to the cooling process of the underlying asthenosphere.

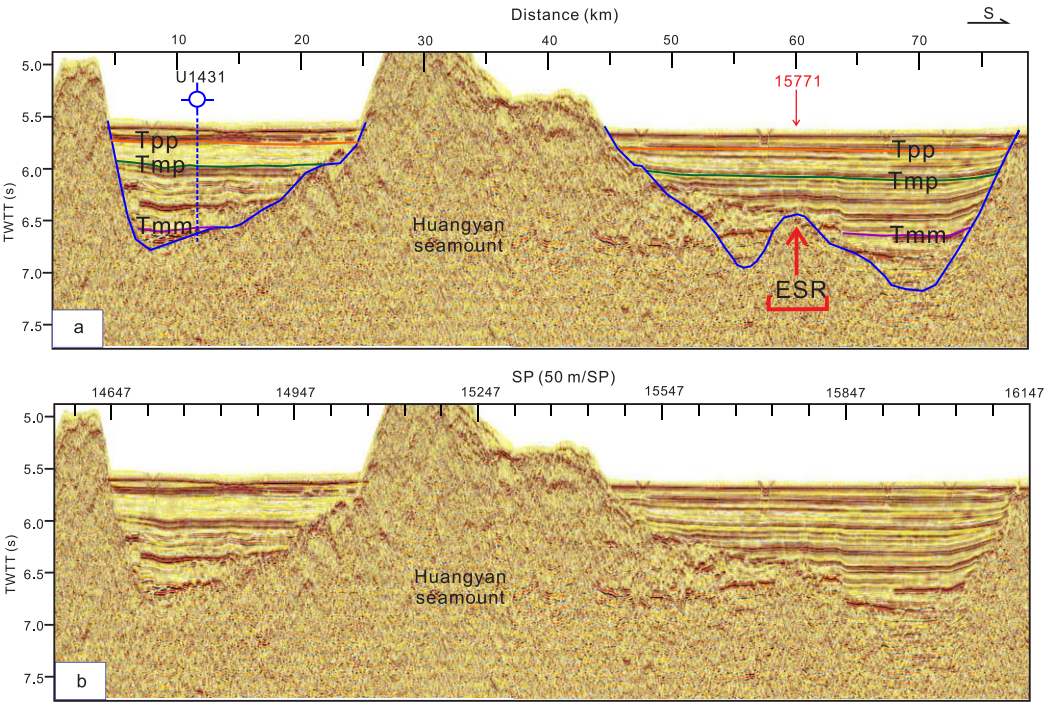

Figure 9. MCS Profile 973SCSIO1 with the extinct spreading ridge (ESR) underlined by a red arrow (shot #15771). The profile location appears as a pink bold line in Figure 2. Blue circle, IODP Site U1431. Blue lines underline the top of basement. Purple, green, and orange lines are seismic sequence boundaries *Tmm*, *Tmp*, and *Tpp* (Li et al., 2015a). SP, shot points; TWTT, two-way travel time in seconds.

Tmm was defined both in the northern SCS, close to the continent-ocean boundary (COB) and in the central part of the East subbasin (Li et al., 2015a) by correlation with drilling data (Expedition 349 Scientists, 2014). The thickness of sediments above *Tmm* is about 1.0–1.1 s in both areas. Sediments are mostly composed of turbidites with seamount slope failure contributing to the observed sediment package in the central East subbasin. However, *Tmm* is deeper in the central part of the East subbasin (Figure 9) than in the northern SCS, where the age of the oceanic crust is older. Even if the whole amount of sediments and the regional overload of the sediments is larger in the north than in the central part of the East subbasin, the maximum basement depth close to the COB is ~6.8 s (Li et al., 2015a), compared with 7.2 s south of the Huangyan seamount (Figure 9), near OBS07 location, at the intersection of Profiles P3 and P4 (Figure 8a and 8b). Additional information comes from the OBS1993 refraction profile (located in Figure 1), where the crust near the northern COB is 6–7 km thick between their OBS14 and OBS15 and thus is typical oceanic crust (Yan et al., 2001). This means that in the whole SCS the thin oceanic crust is only identified in the area of our refraction survey. Now the two important questions are: what is the shape and extent of the thin oceanic domain located in the central part of the East subbasin, before postspreading volcanism occurred? Are the two magmatic systems different during seafloor spreading (magma poor) and postspreading (magma rich) phases?

During the last phase of SCS opening, about 150 km of oceanic crust was created in the central part of the East subbasin, following a N145° spreading direction (Li et al., 2002; Sibuet et al., 2016; Figure 8c). Our wide-angle seismic reflection and refraction data show that, outside the postspreading volcanoes, the basement of typical oceanic crust is shallower than thin oceanic crust. Where the oceanic crust is thin (<5 km, green segments in Figures 3, 8a, and 8b), due to isostatic readjustment, the basement might be deeper than for typical oceanic crust (5–6 km, yellow segments in Figures 3, 8a, and 8c) and due to turbiditic deposition, the thickness of sediments on seismic profiles always exceeds 1.2 s (Figures 3 and 9). Thus, if there is a relationship between sediment thickness and basement depth, one might be able to use the image of sediment layer as a proxy for crustal thickness. In order to map the geographical extent of the thin oceanic crust, we have assumed that where the thickness of sediments is equal or larger than 1.2 s, the oceanic crust is thin.

Short purple line segments in Figures 8b show where the sediment thickness exceeds 1.2 s TWTT on the 18 single-channel seismic profiles acquired during the OBS shooting lines located in Figure 8d. Even if the geographical extent of the thin crust before the postspreading volcanism is difficult to establish, it might correspond to a roughly ENE-WSW trending ~80 km wide zone, which not only includes the two basins located on each side of the Zhenbei-Huangyan seamounts chain but also the area of the postspreading seamounts. This zone is located inside the 150 km wide strip of the last N145° oriented phase of seafloor spreading. The two ENE-WSW lines defining the envelope of the ~80 km wide zone roughly follow the 295 mGal yellow/orange boundary on the Bouguer map (Figure 8b), which defines the boundary between seamounts identified with an intrusive root on refraction data for low Bouguer anomalies, and oceanic domain including minor topographic features without roots for high Bouguer anomalies. Thus, the proposed correlation between sediment and crustal thicknesses suggests that the thin oceanic crust is present north and south of the Zhenbei-Huangyan seamounts Chain B and at the emplacement of postspreading seamounts before their formation (Figure 8b).

4.2. Location of the Extinct Spreading Ridge in the East Subbasin

The determination of the exact location of the ESR is difficult to assess because seafloor spreading magnetic anomalies have been overprinted by magnetic anomalies created by the postspreading volcanism. If one ignores these postspreading seamounts, then indeed the symmetry in the magnetic map of Figure 8c is striking. In addition to refraction data, we use gridded magnetic anomaly, swath-bathymetric, gravity maps and MCS profiles to determine where is the exact location of the ESR.

A first indication of approaching an ESR may be a gradual decrease in crustal thickness, as observed in the Norway Basin (Breivik et al., 2006). It might indicate that the location of OBS07, where the crust is the thinnest along both perpendicular Profiles P3 and P4 (Figures 4, 8a, and 8b), is on or close to the East subbasin ESR. Figure 8c shows the magnetic contoured map with magnetic picks used by Li et al. (2015b) to identify and date magnetic lineations (Li et al., 2015b). Their hypothesis is that all identified magnetic lineations from C6 to C5c are parallel to the orientation of the Zhenbei-Huangyan seamounts chain that was emplaced along a former E-W trending ESR. However, looking in detail at magnetic picks of Li et al. (2015b) in between the two clear and indisputable E-W trending lineations C6 that we have underlined by thick white dashed lines in Figure 8c, the E-W directions of their lineations are questionable: (1) the four eastern picks of their lineation C5e north follow a ~N055° negative trend but the three westernmost picks correspond to the postspreading Zhangzhong seamount negative magnetic anomaly, and have consequently no relationship with the four eastern picks; (2) the two western picks of their lineation C5d north do not follow the same magnetic trend than the two eastern picks; (3) the two picks of their lineation C5c do not belong to the same magnetic lineation, one corresponding to a positive anomaly, the other one to a negative anomaly and are N055° trending.

We have identified positive N055° oriented magnetic trends on the Li et al. (2015b) magnetic map of Figure 8c (thick white dashed lines). If we assume these magnetic trends were continuous during the last spreading phase, i.e., before postspreading volcanism started, and if we assume that there is no significant ridge jump, our proposed location of the ESR (yellow thick dashed line) would be the axis of symmetry of N055° trends. In its western part, the proposed ESR follows a relative negative trend of the magnetic map and passes through the location of OBS07. In its eastern part, the ESR prolongation cuts across the seamount associated with the Huangyan island. Figure 9 further confirms the proposed position of the ESR, south of the Huangyan seamount (Figure 2), probably as a ~500 m high ridge or seamount, as expected at ultraslow and slow spreading rates, where the lithosphere is cold (e.g., the Southwest Indian Ridge, Cannat et al., 1999). At shot #15771 location, the ridge displays onlapping sedimentary layers on its southern side (including *Tmm*), demonstrating that the ESR was emplaced before the postspreading volcanism started. Thus, the location of ESR is determined within the thin oceanic crust domain, where the crust might be the more easily broken.

The estimation of the location of the ESR is quite important not only to identify more accurately magnetic lineations in order to model and date them but also to determine if, as for other slow spread lithosphere, conjugate ridge flanks could present quite different crustal structure and morphology, particularly when detachment faulting operates. Figure 8c shows the seismic coverage is biased toward the northern ridge flank. However, as the boundaries of the 80 km wide zone are located inside the seismic coverage (Figures

8b and 8d), these boundaries seem to be properly located. The only exception concerns the southwestern end of the ESR, which extends outside the strip over 10 km in direction of the Zhongnan faults zone.

4.3. Age of Postspreading Volcanism in the Central East Subbasin

Postspreading basaltic seamount samples collected in the vicinity of the ESR in the East and SW subbasins have been dated by using the K/Ar method (Figure 1). Ages range from 11 to 6 Ma with the exception of Zhongnan seamounts (3.5 Ma; Figure 1). Accurate $^{40}Ar/^{39}Ar$ dating on numerous samples recently collected along the flanks of the postspreading seamounts of the central part of the East subbasin and at IODP Site U1431 displays coherent ages ranging from 6 to 10 Ma (Lin et al., 2016). At IODP Site U1431, the late Miocene sedimentary Unit VI consisting of volcaniclastic breccias and turbidites was dated by Anthony A. P. Koppers (Expedition 349 Scientists, 2014) using the $^{40}Ar/^{39}Ar$ incremental heating method at 8.4–9.9 Ma, with the vast majority of that unit being deposited in a very short period around 9.1 Ma. Clasts in the breccias are angular to subrounded, up to 8 cm in size, and are dominantly basaltic volcanic rocks derived from a local source, probably the Huangyan seamount or the Zhenbei seamount.

Figure 9 shows turbiditic layers onlapping the northern flank of the Huangyan seamount. They are slightly deformed above the *Tmm* sequence boundary (~11.1 Ma). On the contrary, the turbiditic layers at the contact with the southern flank of the Huangyan seamount are largely deformed, but only within the sedimentary section younger than the *Tmm* sequence boundary and older than the *Tmp* sequence boundary (~5.2 Ma). A detailed inspection of the shape of the highly reflective sedimentary sequence located just beneath the *Tmp* sequence boundary shows that the uplift of the Huangyan seamount may have stopped ~6–8 Ma ago, giving an approximate age for the end of emplacement of the Huangyan seamount and it coincides with the termination of sedimentation in the volcaniclastic seamount apron as recorded by the $^{40}Ar/^{39}Ar$ dating.

Consequently, the three methods to date the postspreading volcanism are coherent and complementary, suggesting that the emplacement of the E-W postspreading seamounts of the central part of the East subbasin occurred 6–10 Ma ago, through an extremely thin (3–4 km) oceanic crust, as demonstrated above. It confirms that the E-W Zhenbei-Huangyan seamounts chain (Chain B) was emplaced after seafloor spreading stopped in the SCS, sometime between 13 and 20 Myr ago. Accordingly, the associated E-W negative magnetic lineation is not a seafloor spreading magnetic lineation, though it has been extensively used, simultaneously with the two E-W oriented C6c lineations, to force the identification of intermediate magnetic lineations C5c and C5d to be E-W aligned (Figure 8c).

4.4. Why Thin Oceanic Crust Only Formed in the Central East Subbasin?

Ninety percent of the total volume of postspreading volcanism formed in the SCS where the crust is thin and easier to break compared to the typical oceanic crust. However, the existence of thin crust only in the central part of the East subbasin in the SCS is difficult to assess. Among the hypotheses for the formation of such a thin crust: (1) an episode of low asthenospheric temperatures occurring during early to middle Miocene is a possibility, but its origin remains unknown and (2) a change in the melt delivery pattern associated with a change in spreading direction or rate is a possible explanation. First, such a change is not linked to the postspreading magmatic phase, because we have demonstrated that, contrary to what was thought even recently (e.g., Barckhausen et al., 2014; Briais et al., 1993; Li et al., 2014), this magmatic phase does not occur before the end of spreading but several Myr after the SCS opening. Second, it is not linked to an early to middle Miocene change in seafloor spreading direction during the N145° phase of seafloor spreading because there is no obvious change in spreading directions on the swath-bathymetric map of Figure 8d, occurring since the beginning of the formation of the 150 km wide N055° oriented strip (Sibuet et al., 2016). One possibility, however, is a change in spreading rate at the beginning of the formation of the 80 km wide zone inside the 150 km wide strip.

4.5. N-S Extension and Emplacement Model of Volcanic Seamounts During the Postspreading Phase

From the presence of orthogonal Chains A and B, it is impossible to tell if the extension is N-S or E-W. However, three N-S postspreading FZs marked by red ovals were identified within the N055° spreading strip in Sibuet et al. (2016, Figure 8a). They cut across N055° oriented spreading features. These FZs are not extensional features linked to a tensional episode due for example to a slab pull effect of the Manila slab (Morley, 2016) as they do not present the morphology of normal faults.

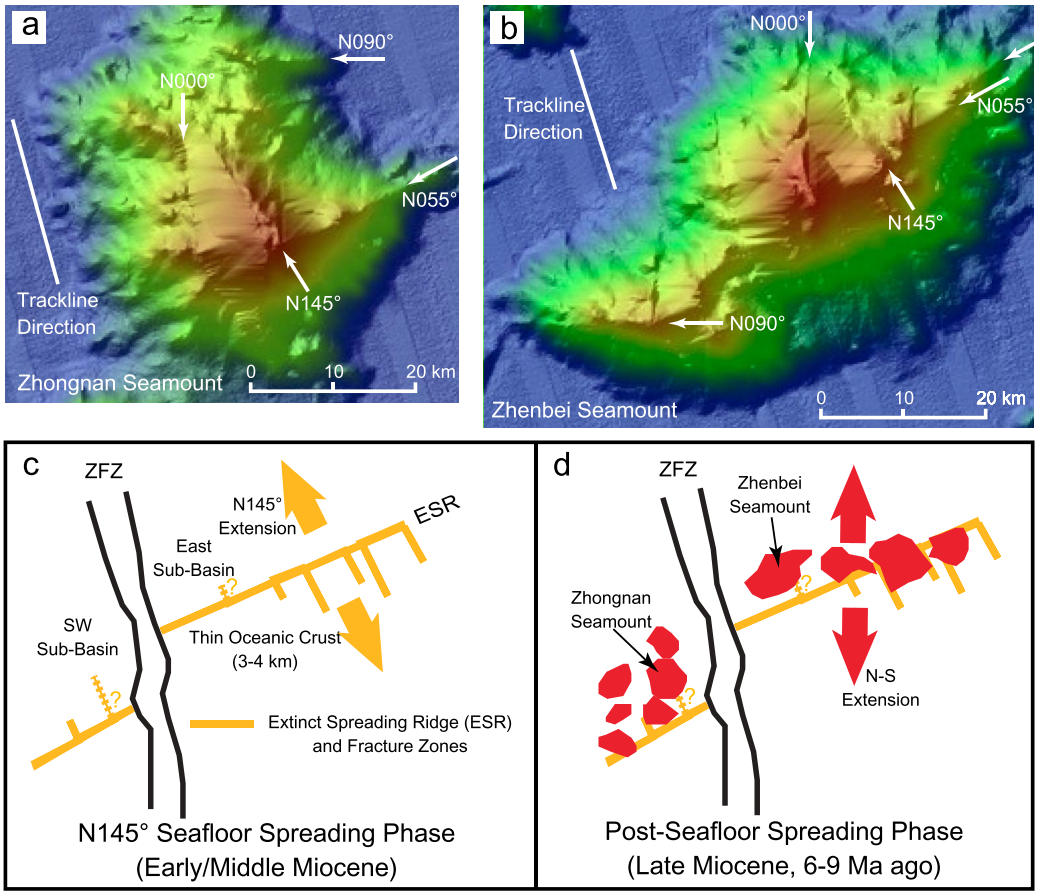

Figure 10. Detailed swath-bathymetric maps of the two (a) Zhongnan and (b) Zenbei seamounts and (c, d) conceptual model of the emplacement of the postspreading volcanic seamounts. The two Zhongnan and Zenbei seamounts (ZN and ZB in Figure 1) are located on each side of the Zhongnan faults zone (ZFZ). In Figures 10a and 10b, conjugate N055° and N145° trends and conjugate E-W and N-S trends correspond to the directions of spreading lineaments and FZs of the last SCS seafloor spreading phase and to the direction perpendicular and parallel to the postspreading extension, respectively. In Figures 10c and 10d, the extinct spreading ridge (ESR) is offset by FZs with small horizontal offsets of unknown sense. Postspreading volcanoes in red are mostly formed at the intersection of the ESR and FZs.

Structural trends of postspreading volcanoes recognized on detailed swath-bathymetric data provide important tectonic constraints. In the N-S Chain A, some seamounts, as the Zhongnan seamount, display more or less round shapes with two sets of conjugate trends: E-W and N-S, and N055° and N145° (Figure 10a). East of the Zhongnan faults zone, individual seamounts of the E-W Chain B also display the same conjugate trends as for the Zhenbei seamount (Figure 10b). These trends are not artifacts as swath-bathymetric track lines observed in the surrounding abyssal plain are oriented N165°. They are oblique to the identified conjugate directions. Hence, the occurrences of spreading conjugate trends (N055° and N145° trends) in the oceanic basement and postspreading conjugate trends (E-W and N-S) in the morphology of postspreading volcanoes belonging to the orthogonal Chains A and B (Figures 10a and 10b) confirm the involvement of simultaneous N145° and N-S directions of extension during the postspreading phase, but also their significant role in the formation of individual seamounts and chains of seamounts A and B.

A geological model where postspreading volcanoes are formed on both sides of the Zhongnan faults zone with respect to the location of the N055° trending ESR is presented in Figures 10c and 10d. Swath-bathymetric data displayed in Sibuet et al. (2016) show that the N145° trending FZs disappear at the contact with postspreading volcanoes located near the ESR. Due to the presence of sediments, these FZs are only identified along short segments, even if they may be longer. As magnetic lineations are mostly continuous (Figure 8c), the FZ horizontal offsets are probably small. The sense of horizontal offsets shifting the ESR is unknown and arbitrarily chosen in Figure 10c. Postspreading volcanoes formed 6–10 Ma ago were

emplaced several Myr after the cessation of seafloor spreading (Figure 10d), In the model, basaltic seamounts were formed during the postspreading N-S tensional phase, obliquely with respect to the ESR located inside the 80 km wide zone of thin oceanic crust considered as a zone of weakness. The rupture of the thin brittle oceanic crust occurred where the crust was the weakest, that is at the intersection of the ESR and N145° trending FZs. N055° and N145° and E-W and N-S conjugate features observed in the morphology of seamounts (Figures 10a and 10b) were simultaneously active during the formation of these seamounts.

5. Mechanism of Postspreading Volcanism in the South China Sea

The origin of enriched (E)-MORB type basalts is generally suggested to be due to plume-ridge interactions based on compositional variations of MORB toward hotspots as in the Iceland, Azores, or Bouvet examples (Dosso et al., 1993; Roex et al., 1992; Schilling et al., 1983; Taylor et al., 1997). However, the occurrence of E-type MORBs can have different origins that are not necessarily associated with mantle plume activity (e.g., Niu et al., 1999; Prinzhofer et al., 1989; Zhang et al., 2012). In this paper, we have established that for the SCS almost all of the postspreading volcanism occurred 6–10 Ma ago close to the East and SW subbasins extinct spreading ridges and a N-S phase of extension, which is oblique with respect to the N145° oriented last seafloor spreading phase. A few postspreading seamounts display K/Ar ages possibly a little bit older as Zhangzhong (ZZ) and Zhiyou (ZY) seamounts (11–6 Ma; Pautot et al., 1990) or younger as Zhongnan (ZN) seamount (3.5 Ma; Tu et al., 1992; Figure 1) but K/Ar ages of seamounts are always suspect due to a high likelihood of those samples being altered hydrothermally or by seawater. Important questions we raise are: What is the origin of the postspreading phase of extension? Is the postspreading volcanism related to the Hainan plume and, if we assume that is likely, when did the Hainan plume started to be active?

5.1. Hainan Plume Influence?

Recent tomographic images (e.g., Xia et al., 2016) suggest a continuous low-velocity anomaly characterized by a columnar tail with a diameter of 200–300 km extending from a depth of 1,100 km in the lower mantle to the upper mantle where it spreads laterally (plume head) and feeds a magmatic pool located in the upper mantle. Further upward, small conduits seem to feed a secondary magmatic pool located in the lithosphere and at the origin of the postspreading volcanism (Xia et al., 2016). Even if the detailed geometry of the Hainan plume is presently debated, all tomographic images show that a continuous low velocity zone is rising from the lower mantle to the base of the crust (e. g., Huang, 2014; Huang & Zhao, 2006; Lei et al., 2009).

Basalts in Hainan Island, Leizhou Peninsula, and SE Vietnam are mainly alkali ocean island basalts (OIBs) with EM2-type (enriched mantle end-member from an enriched mantle source (e.g., Zou & Fan, 2010). The OIB-type intraplate volcanism with an EM2-like enriched mantle source end-member could have been originated from the Hainan plume (An et al., 2017; Xu et al., 2012). $^{40}Ar/^{39}Ar$ dating indicates that the Cenozoic volcanism in Hainan Island and Leizhou Peninsula started in the late Miocene (~13 Ma; Wang et al., 2013). In south Vietnam, $^{40}Ar/^{39}Ar$ dating on 41 samples show that the first stage of igneous activity is from the very beginning of middle Miocene (16 Ma; Lee et al., 1998), began ~17 Ma ago and continues until today, mostly along the offshore margin (Hoàng et al., 2013), but is restricted in another study to an age range from 13.8 to 4.1 Myr (An et al., 2017). Thus, these basaltic samples are all younger than 17 Myr, suggesting that the influence of the Hainan plume might have started ~17 Ma ago.

The basalts of the South China Sea seamounts generally have OIB-type alkali basalts and EM2-type mantle sources (Tu et al., 1992; Yan et al., 2008a, 2008b; Zhang et al., 2017), which constitute the geochemical evidence for the influence of the Hainan plume. The influence of the Hainan plume may be recorded at IODP hole U1431E, where $^{40}Ar/^{39}Ar$ dating indicates that the basalts recovered at the base of the drilling hole are ~15 Ma for the upper pillow lava flow (Core 41R) and ~15.5 Ma for the lower massive lava flow series (Core 47R; Koppers, 2014). From Os and Nd isotope compositions of these two lava flows, Tejada et al. (2016) show that an enriched mantle end-member in the source of Site U1431E basalts is consistent with the involvement of a melting anomaly, previously suggested to be a plume mantle, during the latest phase of spreading. An important observation is that Zhang et al. (2017) found carbonatite-alkali basalt series in the 6–8 Myr postspreading volcanic breccia at Site U1431. These volcanic breccias were suggested to have a mantle source of carbonated eclogite, which is in concert with the petrologic observation of Wang et al. (2013) that also suggested an eclogitic mantle source derived from recycled oceanic crust. Concerning the

postspreading volcanism in the SCS, it is mainly composed of alkali basalts displaying E-MORB type basalt geochemical characteristics, which may be also interpreted as linked to the Hainan plume (e.g., Yan et al., 2008a). If these assumptions are correct, the Hainan plume may have been active in the SCS at least since 15 Ma ago at IODP Site U1431 and recorded from 6 to 10 Ma ago with a possible period of inactivity in between these two events.

5.2. Hainan Plume Proxies

In the northern Galapagos volcanic province (Mittelstaedt et al., 2012; Sinton et al., 2003), postspreading volcanism was emplaced obliquely to the direction of the active spreading axis located north of the Galapagos plume. Here lavas from Wolf and Darwin islands have experienced petrogenetic histories with geochemical evidence of contributions from the Galapagos mantle plume (E-MORB type basalts; Harpp et al., 2014). Other examples of postspreading volcanism emplaced along a former ESR shortly after spreading ceased and distal from any mantle plume are well documented, as for the Davidson Seamount (Castillo et al., 2010; Clague et al., 2009) and the Antarctic-Phoenix Ridge (Choe et al., 2007; Haase et al., 2011; Livermore et al., 2000). Postspreading magmatism is not unusual, particularly in areas underlain by mantle containing enriched heterogeneities. Both Castillo et al. (2010) and Haase et al. (2011) propose for Davidson seamount and Phoenix Ridge that the source consists of enriched mantle portions embedded in a depleted mantle. Because a large degree of partial melting produces N-MORB type seafloor spreading basalts, whereas a small degree of melting tends to produce enriched melts, only segments of extinct spreading ridges underlain by such enriched and fertile mantle are likely to produce postspreading volcanism because of the low degree of melting relative to a normal spreading ridge (Haase et al., 2011). The low degree of partial melting beneath these recently abandoned spreading centers have been interpreted as resulting from a buoyancy-driven decompression melting of the lithospheric and asthenospheric mantle material beneath active spreading centers (Castillo et al., 2010). This enriched components that preexist in the depleted mantle could also have been derived from contamination of a mantle plume (e.g., Zhang & Li, 2016).

5.3. Comparison Between Different Postspreading Volcanisms

Based on the crustal velocity structure, the correlation between the average lower crustal velocities (*V*p) and crustal thickness (H; Figure 11) was established. If the off-axis volcanism results from a mantle plume activity with elevated mantle temperature, high melting degrees are expected with a positive H-*V*p correlation ($\chi = 1$; Holbrook et al., 2001). Figure 11 shows a very limited, but steady increase of *V*p with H, certainly for the Huangyan seamount and for portions of Zhenbei seamount. This correlation indicates that the postspreading volcanism is most likely related to multiple low-degree melting events and thus the elevated mantle temperature caused by the Hainan plume was a minor factor at the time of emplacement of postspreading volcanism, 6–10 Ma ago. Below the two Zhenbei and Huangyan seamounts (Figure 4), the thick crust as well as the high-velocity values could be interpreted as late intrusives mostly located in layer 3 (Figure 5). Thus, the formation mechanism of the seamounts chain might be explained by the buoyancy-driven decompression melting mechanism (Castillo et al., 2010; Wang et al., 2016) occurring independently beneath each seamount as supported by numerical modeling (Meng & Zhang, 2014).

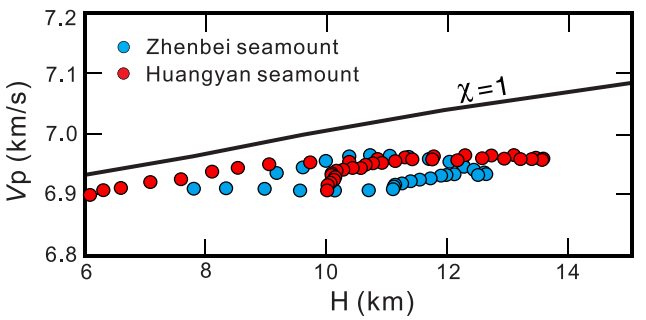

Figure 11. Crustal thickness (H) versus average lower crustal velocity (*V*p) for the Zhenbei (blue dots) and Huangyan (red dots) seamounts calculated from velocity models in Figure 4 along Profile P2 (located in Figure 2) with sampling interval of 1 km. The $\chi = 1$ black line represents passive decompression melting of normal mantle. To estimate the in situ conditions, we use a pressure correction of 0.00022 km/s/MPa and a temperature correction of −0.0005 km/s/°C with a linear gradient from 10°C at the seafloor to 750°C at a depth of 40 km (Holbrook et al., 2001).

In the East subbasin, the E-W Chain B is 55° oblique with respect to the direction of the ESR. In the northern Galapagos volcanic province, the Wolf-Darwin lineament (WDL) also is 40° oblique with respect to the spreading direction (Mittelstaedt et al., 2012). Here Wolf Island was formed ~1.6 Ma ago on a 3–4 Ma old oceanic crust and Darwin Island ~0.4 Ma ago on a 2–3 Ma old oceanic crust (Harpp & Geist, 2002), with the present-day spreading axis being approximately located 200 km north of the Galapagos plume located beneath Fernandina and Isabela Islands. Thus, from a geometrical point of view, the Galapagos system could be considered as a proxy of the Hainan plume system, with similar angles for spreading and postspreading features (40° compared with 55°), a distance to the plume still in the 1,000 km radius of a mantle plume influence (200 km compared with

700 km) and a time delay between the age of underlying oceanic crust and postspreading features varying from ~2 Myr compared with ~4–11 Myr (if the end of spreading occurred 13–20 Ma ago), respectively.

On the contrary, the Davidson Seamount (Clague et al., 2009) and the Antarctic-Phoenix Ridge (Livermore et al., 2000) display postspreading features emplaced along former ESRs, suggesting that it might be difficult, even impossible, to find postspreading features making a significant angle with spreading directions outside a plume influence. It is interesting to observe that the Hainan plume upwelled much earlier than the 6–10 Myr postspreading magmatism. Even if we do not know when the SCS opening ended, sometime between 13 and 20 Myr (Barckhausen et al., 2014; Briais et al., 1993; Li et al., 2014), the SCS was small and the bulk of the plume was erupted below the continental crust in the vicinity of Hainan Island and below the northern SCS continental margin, through a relatively thick continental crust. Hence, the Hainan plume magmatism was mostly inefficient, that is, some of the plume materials were not directly erupted/intruded, polluting the upper mantle as proposed by the interpretation of tomographic data (Xia et al., 2016). For this reason, the source of postseafloor spreading alkali magmas could have been produced from the upper mantle that was polluted by the Hainan mantle plume component. The buoyancy-driven partial melting model (Castillo et al., 2010) may be the correct model to produce the 6–10 Myr postseafloor spreading magmatism.

To summarize, the enriched heterogeneities most likely formed because the upper mantle was previously contaminated or metasomatized by the Hainan plume, which is consistent with the current geophysically anomalous feature of the mantle in the SCS region. Buoyancy-driven upwelling is probably the best mechanism to create postspreading magmatism, because Hainan plume materials are enriched and thus, the more fusible component located in the underlying mantle. Our preferred interpretation is not unique, but is consistent with both the nondirect influence of the Hainan plume (based on geophysics and tectonics), and the Hainan plume geochemical signature in the lavas. The arguments presented here are rather in favor of an influence of the Hainan plume in a N-S tensional context. An indisputable way to solve the problem would be to establish, by a careful and significant study, if specific geochemical analyses could be able to undoubtedly demonstrate in the future the potential influence of the Hainan plume in the geochemistry of postspreading volcanism.

6. Conclusions

The main key points of this study are as follows:

Thirty-eight OBSs were deployed along four profiles in the central part of the East subbasin, in the area of the Zhenbei and Huangyan seamounts. *P* wave velocity models were determined by forward modeling using the *Rayinvr* code and joint refraction and wide-angle reflection travel time inversion using the *Tomo2d* code. The crust in the central East subbasin has been divided into four types of crust, the thin oceanic crust (<5 km), the typical oceanic crust (5–6 km), the thick oceanic crust hosting postspreading volcanism (>6 km) with significant intrusive roots and the thick oceanic crust with enhanced spreading features (>6 km) but without significant roots. Crustal thicknesses beneath the Zhenbei and Huangyan seamounts are up to 12.0 and 13.2 km. Composed of extrusives in their upper part, the root of these volcanoes is characterized by high-velocity values, which may correspond to late intrusive bodies.

Based on seismic reflection and refraction data, and gravity anomalies, the thin oceanic crust domain (<5 km), which includes the extinct spreading ridge (ESR), has been defined as a ~80 km ENE-WSW oriented wide zone. This zone is located inside the 150 km wide strip oriented N055° and corresponding to the last phase of opening of the SCS. This thin oceanic crust is most susceptible to deformation and can be most easily penetrated when late postspreading volcanism is emplaced.

On each side of the Zhongnan faults zone, N-S FZs trends and postspreading volcanic features emplaced along both N-S and E-W directions suggest they belong to a postspreading N-S phase of extension of only a few kilometers in amplitude. The presence of simultaneous seafloor spreading (N055° and N145°) and postspreading (N000° and N090°) features in the morphology of some of these volcanoes, as well as the E-W alignment of these volcanoes in the central East subbasin, show that the rupture of the brittle oceanic crust focused where the thin oceanic crust was the weakest, i.e., at the intersection of the ESR with former seafloor spreading FZs. The mechanism of seamounts emplacement involves previous seafloor spreading

zones of weaknesses and trends of the new phase of extension but also the E-W alignment of postspreading volcanoes occurring obliquely with respect to the N055° oriented ESR.

The Hainan plume magmatism was mostly inefficient because the plume is located below the continent and below the northern SCS continental margin, where the continental crust is still relatively thick. Hence, we postulate that most of the plume materials were not directly erupted/intruded but were polluting the upper mantle as supported by tomographic evidence. Thus, the source of postseafloor spreading alkali magmas could have been from the upper mantle polluted by the Hainan mantle plume component and the buoyancy-driven upwelling is probably the best mechanism to create postspreading magmatism. Our interpretation is not unique, but is consistent with both the nondirect influence of the Hainan plume (based on geophysics and tectonics), and the Hainan plume geochemical signature in the lavas.

Acknowledgments
We thank the crew of the *R/V* Shiyan 2 as well as scientists and technicians for their precious involvement during the cruise. Thanks to Zhen Sun, Ning Qiu, and Litian Hu for kindly providing MCS data and the Bouguer anomaly map. We are particularly grateful to Donna Blackman, Paterno R. Castillo, Anthony A. P. Koppers, and Thorsten Becker for their careful reviews and scientific suggestions, which help to improve the manuscript. We acknowledge insightful discussions with Jian Lin, Hongfeng Yang, Chunfeng Li, Min Xu, Ting Yang, and particularly Anthony A. P. Koppers, Paterno R. Castillo, and Guoliang Zhang who carefully reviewed the latest version of the revised paper and Timothy M. Kusky who kindly edited the last version of the paper. The GMT software (Wessel & Smith, 1995) was used in this study. This work is supported by the Chinese National Natural Science Foundation (contracts 91428204, 91028002, 41730532, 41674092, and 41576070). All OBS data shown in this paper can be downloaded at https://pan.baidu.com/mbox/homepage#share/type=session.

References

An, A. R., Choi, S. H., Yu, Y., & Lee, D. C. (2017). Petrogenesis of Late Cenozoic basaltic rocks from southern Vietnam. *Lithos*, *272–273*, 192–204. https://doi.org/10.1016/j.lithos.2016.12.008

Barckhausen, U., Engels, M., Franke, D., Ladage, S., & Pubellier, M. (2014). Evolution of the South China Sea: Revised ages for breakup and seafloor spreading. *Marine and Petroleum Geology*, *58*, 599–611. https://doi.org/10.1016/j.marpetgeo.2014.02.022

Breivik, A. J., Mjelde, R., Faleide, J. I., & Murai, Y. (2006). Rates of continental breakup magmatism and seafloor spreading in the Norway Basin–Iceland plume interaction. *Journal of Geophysical Research*, *111*, B07102. https://doi.org/10.1029/2005JB004004

Briais, A., Patriat, P., & Tapponnier, P. (1993). Updated interpretation of magnetic anomalies and seafloor spreading stages in the South China Sea: Implications for the Tertiary tectonics of Southeast Asia. *Journal of Geophysical Research*, *98*(B4), 6299–6328.

Cannat, M., Rommevaux-Jestin, C., Sauter, D., Deplus, C., & Mendel, V. (1999). Formation of the axial relief at the very slow spreading Southwest Indian Ridge (49° to 69°E). *Journal of Geophysical Research*, *104*(B10), 22825–22843.

Castillo, P. R., Clague, D. A., Davis, A. S., & Lonsdale, P. F. (2010). Petrogenesis of Davidson seamount lavas and its implications for fossil spreading center and intraplate magmatism in the eastern Pacific. *Geochemistry Geophysics Geosystems*, *11*, Q02005. https://doi.org/10.1029/2009GC002992

Choe, W. H., Lee, J. I., Mi, J. L., Hur, S. D., & Jin, Y. K. (2007). Origin of E-MORB in a fossil spreading center: The Antarctic-Phoenix ridge, Drake Passage, Antarctica. *Geosciences Journal*, *11*(3), 185–199.

Clague, D. A., Paduan, J. B., Duncan, R. A., Huard, J. J., Davis, A. S., Castillo, P. R., et al. (2009). Five million years of compositionally diverse, episodic volcanism: Construction of Davidson Seamount atop an abandoned spreading center. *Geochemistry Geophysics Geosystems*, *10*, Q12009. https://doi.org/10.1029/2009GC002665

Dosso, L., Bougault, H., & Joron, J.-L. (1993). Geochemical morphology of the North Mid-Atlantic Ridge, 10°–24°N: Trace element-isotope complementarity. *Earth and Planetary Science Letters*, *120*(3), 443–462.

Expedition 349 Scientists. (2014). *South China Sea tectonics: Opening of the South China Sea and its implications for southeast Asian tectonics, climates, and deep mantle process since the late Mesozoic* (Preliminary Rep. 349). La Jolla, CA: International Ocean Discovery Program. https://doi.org/10.14379/iodp.pr.349.2014

Franke, D., Savva, D., Pubellier, M., Steuer, S., Mouly, B., Auxiètre, J.-L., et al. (2014). The final rifting evolution in the South China Sea. *Marine and Petroleum Geology*, *58*, 704–720. https://doi.org/10.1016/j.marpetgeo.2013.11.020

Gradstein, F. M., Ogg, J. G., & Smith, A. G. (Eds.). (2005). *A geologic time scale 2004*. Cambridge, UK: Cambridge University Press. https://doi.org/10.1017/CBO9780511536045

Haase, K. M., Beier, C., Fretzdorff, S., Leat, P. T., Livermore, R. A., Barry, T. L., et al. (2011). Magmatic evolution of a dying spreading axis: Evidence for the interaction of tectonics and mantle heterogeneity from the fossil Phoenix Ridge, Drake Passage. *Chemical Geology*, *280*(1–2), 115–125.

Hall, R. (2002). Cenozoic geological and plate tectonic evolution of SE Asia and the SW Pacific: Computer-based reconstructions, models and animations. *Journal of Asian Earth Sciences*, *20*(4), 353–431.

Harding, A. J., Kent, G. M., & Orcutt, J. A. (1993). A multichannel seismic investigation of upper crustal structure at 9°N on the East Pacific Rise: Implications for crustal accretion. *Journal of Geophysical Research*, *98*(B8), 13925–13944. https://doi.org/10.1029/93JB00886

Harpp, K., & Geist, D. (2002). Wolf–Darwin lineament and plume–ridge interaction in northern Galápagos. *Geochemistry Geophysics Geosystems*, *3*(11), 8504. https://doi.org/10.1029/2002GC000370

Harpp, K. S., Wirth, K. R., Teasdale, R., Blair, S., Reed, L., Barr, J., et al. (2014). Plume-ridge interaction in the Galápagos: Perspectives from Wolf, Darwin, and Genovesa Islands. In K. S. Harpp, E. Mittelstaedt, N. d'Ozouville, & D. W. Graham (Eds.), *The Galapagos: A natural laboratory for the earth sciences*. Hoboken, NJ: John Wiley. https://doi.org/10.1002/9781118852538.ch15

He, E. Y., Zhao, M. H., Qiu, X. L., Sibuet, J.-C., Wang, J., & Zhang, J. Z. (2016). Crustal structure across the post-spreading magmatic ridge of the East sub-basin in the South China Sea: Tectonic significance. *Journal of Asian Earth Sciences*, *121*, 139–152. https://doi.org/10.1016/j.jseaes.2016.03.003

Hoàng, N., Flower, M. F. J., Chí, C. T., Xuân, P. T., Quý, H. V., & Son, T. T. (2013). Collision-induced basalt eruptions at Pleiku and Buôn Mê Thuột, south-central Viet Nam. *Journal of Geodynamics*, *69*, 65–83.

Holbrook, W. S., Larsen, H. C., Korenaga, J., Dahl-Jensen, T., Reid, I. D., Kelemen, P. B., et al. (2001). Mantle thermal structure and active upwelling during continental breakup in the North Atlantic. *Earth and Planetary Science Letters*, *190*(3–4), 251–266.

Hsu, S.-K., Armada, L., Doo, W.-B., & Yeh, Y.-C. (2016). *New insight on the opening of the South China Sea basin*. Paper presented at EGU General Assembly 2016, Geophysical Research Abstracts (Vol. 18, EGU2016–4303), Vienna, Austria.

Huang, J. (2014). P- and S-wave tomography of the Hainan and surrounding regions: Insight into the Hainan plume. *Tectonophysics*, *633*(1), 176–192. https://doi.org/10.1016/j.tecto.2014.07.007

Huang, J., & Zhao, D. (2006). High-resolution mantle tomography of China and surrounding regions. *Journal of Geophysical Research*, *111*, B09305. https://doi.org/10.1029/2005JB004066

Ishihara, T., & Kisimoto, K. (1996). *Magnetic anomaly map of East Asia* (1:4,000,000, CD-ROM Version). Tokyo, Japan: Geological Survey of Japan, AIST and Coordinating Committee for Coastal and Offshore Geoscience Programs in East and Southeast Asia (CCOP).

Koppers, A. A. P. (2014). *On the $^{40}Ar/^{39}Ar$ dating of low-potassium ocean crust basalt from IODP Expedition 349, South China Sea*. Paper presented at AGU Fall Meeting 2014 (Abstracts T31E-03). San Francisco, CA: American Geophysical Union.

Korenaga, J., Holbrook, W. S., Kent, G. M., Kelemen, P. B., Detrick, R. S., Larsen, H. C., et al. (2000). Crustal structure of the southeast Greenland margin from joint refraction and reflection seismic tomography. *Journal of Geophysical Research*, *105*(B9), 21591–21614. https://doi.org/10.1029/2000JB900188

Lee, T.-Y., Lo, C.-H., Chung, S.-L., Chen, C.-Y., Wang, P.-L., Lin, W.-P., et al. (1998). $^{40}Ar/^{39}Ar$ dating result of Neogene basalts in Vietnam and its tectonic implication. In M. F. J. Flower, S.-L. Chung, C.-H. Lo, & T.-Y. Lee (Eds.), *Mantle dynamics and plate interactions in East Asia*. Washington, DC: American Geophysical Union. https://doi.org/10.1029/GD027p0317

Lei, J., Zhao, D., Steinberger, B., Wu, B., Shen, F., & Li, Z. (2009). New seismic constraints on the upper mantle structure of the Hainan plume. *Physics of the Earth and Planetary Interiors*, *173*(1–2), 33–50.

Li, C.-F., Li, J., Ding, W., Franke, D., Yao, Y., Shi, H., et al. (2015a). Seismic stratigraphy of the central South China Sea basin and implications for neotectonics. *Journal of Geophysical Research: Solid Earth*, *120*, 1377–1399. https://doi.org/10.1002/2014JB011686

Li, C.-F., Lin, J., Dadd, K. A., Ding, W.-W., Hernández-Almeida, I., Huang, X.-L., et al. (2015b). Site U1431. In C. F. Li, J. Lin, D. K. Kulhanek, & the Expedition 349 Scientists (Eds.), *Proceedings of the International Ocean Discovery Program, 349: South China Sea Tectonics* (Vol. 349, pp. 1–54). College Station, TX: International Ocean Discovery Program. https://doi.org/10.14379/iodp.proc.349.103.2015

Li, C. F., & Song, T. (2012). Magnetic recording of the Cenozoic oceanic crustal accretion and evolution of the South China Sea Basin. *Chinese Science Bulletin*, *57*(24), 3165–3181.

Li, C.-F., Xu, X., Lin, J., Sun, Z., Zhu, J., Yao, Y., et al. (2014). Ages and magnetic structures of the South China Sea constrained by deep tow magnetic surveys and IODP Expedition 349. *Geochemistry Geophysics Geosystems*, *15*, 4958–4983. https://doi.org/10.1002/2014GC005567

Li, J. B., Jin, X. G., & Gao, J. Y. (2002). Morpho-tectonic study on late stage spreading of the eastern sub-basin of South China Sea. *Science in China (Series D)*, *45*(11), 978–989.

Lin, J., Li, C. F., Wang, P., & Kulhanek, D. K. (2016). *Recent multidisciplinary research initiatives and IODP Drilling in the South China Sea*. Paper presented at AGU Fall Meeting 2016 (Abstracts OS53C-01). San Francisco, CA: American Geophysical Union.

Livermore, R., Balanyá, J. C., Maldonado, A., Martínez, J. M., Rodríguez-Fernández, J., Sanz de Galdeano, C., et al. (2000). Autopsy on a dead spreading center: The Phoenix ridge, Drake Passage, Antarctica. *Geology*, *28*(7), 607–610.

Meng, L., & Zhang, J. (2014). The magmatic activity mechanism of the fossil spreading center in the Southwest sub-basin, South China Sea. *Science in China (Series D)*, *44*, 239–249.

Minshull, T. A., & White, R. S. (1996). Thin crust on the flanks of the slow-spreading Southwest Indian Ridge. *Geophysical Journal International*, *125*(1), 139–148. https://doi.org/10.1111/j.1356-246X.1996.tb06541.x

Mittelstaedt, E., Soule, S., Harpp, K., Fornari, D., Mckee, C., Tivey, M., et al. (2012). Multiple expressions of plume-ridge interaction in the Galápagos: Volcanic lineaments and ridge jumps. *Geochemistry Geophysics Geosystems*, *13*, Q05018. https://doi.org/10.1029/2012GC004093

Morley, C. K. (2016). Major unconformities/termination of extension events and associated surfaces in the South China Seas: Review and implications for tectonic development. *Journal of Asian Earth Sciences*, *120*, 62–86. https://doi.org/10.1016/j.jseaes.2016.01.013

Muller, M. R., Robinson, C. J., Minshull, T. A., White, R. S., & Bickle, M. J. (1997). Thin crust beneath ocean drilling program borehole 735B at the Southwest Indian Ridge? *Earth and Planetary Science Letters*, *148*(1–2), 93–107.

Niu, Y., Collerson, K. D., Batiza, R., Wendt, J. I., & Regelous, M. (1999). Origin of enriched-type mid-ocean ridge basalt at ridges far from mantle plumes: The East Pacific Rise at 11°20′N. *Journal of Geophysical Research*, *104*(B4), 7067–7087.

Pautot, G., Rangin, C., Briais, A., Wu, J. L., Han, S. Q., Li, H. G., et al. (1990). The axial ridge of the South China Sea: A seabeam and geophysical survey. *Oceanologica Acta*, *13*(2), 129–143.

Prinzhofer, A., Lewin, E., & Allègre, C. J. (1989). Stochastic melting of the marble cake mantle: Evidence from local study of the East Pacific Rise at 12°50′N. *Earth and Planetary Science Letters*, *92*(2), 189–206.

Roex, A. P. L., Dick, H. J. B., & Watkins, R. T. (1992). Petrogenesis of anomalous K-enriched MORB from the Southwest Indian Ridge: 11°53′E to 14°38′E. *Contributions to Mineralogy and Petrology*, *110*(2–3), 253–268.

Sandwell, D. T., Müller, R. D., Smith, W. H. F., Garcia, E., & Francis, R. (2014). New global marine gravity model from CryoSat-2 and Jason-1 reveals buried tectonic structure. *Science*, *346*(6205), 65–67. https://doi.org/10.1126/science.1258213

Schilling, J.-G., Zapac, M., Evans, R., Johnston, T., White, W., Devine, J. D., et al. (1983). Petrological and geochemical variation along the Mid-Atlantic Ridge from 29°N to 73°N. *American Journal of Science*, *283*, 510–586.

Sibuet, J.-C., Yeh, Y.-C., & Lee, C.-S. (2016). Geodynamics of the South China Sea. *Tectonophysics*, *692*, 98–119. https://doi.org/10.1016/j.tecto.2016.02.022

Sinton, J., Detrick, R., Canales, J. P., Ito, G., & Behn, M. (2003). Morphology and segmentation of the western Galápagos spreading center, 90.5°–98°W: Plume-ridge interaction at an intermediate spreading ridge. *Geochemistry Geophysics Geosystems*, *4*(12), 8515. https://doi.org/10.1029/2003GC000609

Sun, W. D. (2016). Initiation and evolution of the South China Sea: An overview. *Acta Geochim*, *35*(3), 215–225. https://doi.org/10.1007/s11631-016-0110-x

Taylor, R. N., Thirlwall, M. F., Murton, B. J., Hilton, D. R., & Gee, M. A. M. (1997). Isotopic constraints on the influence of the Icelandic plume. *Earth and Planetary Science Letters*, *148*, E1–E8.

Tejada, M. L., Castillo, P., Huang, X. L., & Senda, R. (2016). *Crustal and mantle source inputs in the evolution of the South China Sea*. Paper presented at AGU Fall Meeting 2016 (Abstracts OS53C-06). San Francisco, CA: American Geophysical Union.

Tu, K., Flower, M. F. J., Carlson, R. W., Xie, G., Chen, C. Y., & Zhang, M. (1992). Magmatism in the South China Basin: 1. Isotopic and trace-element evidence for an endogenous Dupal mantle component. *Chemical Geology*, *97*(1–2), 47–63. https://doi.org/10.1016/0009-2541(92)90135-R

Wang, J., Zhao, M. H., Qiu, X. L., Sibuet, J.-C., He, E. Y., Zhang, J. Z., et al. (2016). 3D seismic structure of the Zhenbei-Huangyan seamounts chain in the East sub-basin of the South China Sea and its mechanism of formation. *Geological Journal*, *51*(S1), 448–463. https://doi.org/10.1002/gj.2781

Wang, X. C., Li, Z. X., Li, X. H., Li, J., Xu, Y. G., & Li, X. H. (2013). Identification of an ancient mantle reservoir and young recycled materials in the source region of a young mantle plume: Implications for potential linkages between plume and plate tectonics. *Earth and Planetary Science Letters*, *377–378*(5), 248–259. https://doi.org/10.1016/j.epsl.2013.07.003

Wang, X. J., Wu, M. Q., Liang, D. H., & Yin, A. W. (1984). Some geochemical characteristics of basalts from the South China Sea [in Chinese with English abstract]. *Geochemica*, *4*, 332–340.

Wang, Y. J., Han, X. Q., Luo, Z. H., Qiu, Z. Y., Ding, W. W., Li, J. B., et al. (2009). Late Miocene magmatism and evolution of Zhenbei-Huangyan Seamount in the South China Sea: Evidence from petrochemistry and chronology [in Chinese with English abstract]. *Acta Oceanologica Sinica*, *31*(4), 93–102.

Wessel, P., & Smith, W. H. (1995). New version of generic mapping tools released. *Eos Transactions American Geophysical Union*, *76*(33), 329.
White, R. S., McKenzie, D., & O'Nions, R. K. (1992). Oceanic crustal thickness from seismic measurements and rare earth element inversions. *Journal of Geophysical Research*, *97*(B13), 19683–19715. https://doi.org/10.1029/92JB01749
Wu, J., Suppe, J., Lu, R., & Kanda, R. (2016). Philippine Sea and East Asian plate tectonics since 52 Ma constrained by new subducted slab reconstruction methods. *Journal of Geophysical Research: Solid Earth*, *121*, 4670–4741. https://doi.org/10.1002/2016JB012923
Xia, S. H., Zhao, D. P., Sun, J. L., & Huang, H. B. (2016). Teleseismic imaging of the mantle beneath southernmost China: New insights into the Hainan plume. *Gondwana Research*, *36*, 46–43. https://doi.org/10.1016/j.gr.2016.05.003
Xu, Y. G., Wei, J. X., Qiu, H. N., Zhang, H. H., & Huang, X. L. (2012). Opening and evolution of the South China Sea constrained by studies on volcanic rocks: Preliminary results and a research design. *Chinese Science Bulletin*, *57*(24), 3150–3164. https://doi.org/10.1007/s11434-011-4921-1
Yan, P., Zhou, D., & Liu, Z. (2001). A crustal structure profile across the northern continental margin of the South China Sea. *Tectonophysics*, *338*(1), 1–21.
Yan, Q. S., Shi, X. F., & Castillo, P. R. (2014). The late Mesozoic–Cenozoic tectonic evolution of the South China Sea: A petrologic perspective. *Journal of Asian Earth Sciences*, *85*, 178–201. https://doi.org/10.1016/j.jseaes.2014.02.005
Yan, Q. S., Shi, X. F., Yang, Y. M., & Wang, K. S. (2008b). Potassium-argon/argon-40-argon-39 geochronology of Cenozoic alkali basalts from the South China Sea. *Acta Oceanologica Sinica*, *27*(6), 115–123.
Yan, Q. S., Shi, X. F., Wang, K. S., Bu, W. R., & Xiao, L. (2008a). Major element, trace element, and Sr, Nd and Pb isotope studies of Cenozoic basalts from the South China Sea. *Science in China (Series D)*, *51*(4), 550–566. https://doi.org/10.1007/s11430-008-0026-3
Yao, B. C. (1996). Tectonic evolution of the South China Sea in Cenozoic. *Marine Geology & Quaternary Geology*, *16*(2), 1–13.
Zelt, C. A. (1999). Modelling strategies and model assessment for wide angle seismic travel time. *Geophysical Journal International*, *139*(1), 183–204.
Zelt, C. A., & Smith, R. B. (1992). Seismic traveltime inversion for 2-D crustal velocity structure. *Geophysical Journal International*, *108*, 16–34.
Zhang, G. L., Chen, L. H., Jackson, M. G., & Hofmann, A. W. (2017). Evolution of carbonated melt to alkali basalt in the South China Sea. *Nature Geoscience*, *10*(3), 229. https://doi.org/10.1038/ngeo2877
Zhang, G. L., & Li, C. (2016). Interactions of the Greater Ontong Java mantle plume component with the Osbourn Trough. *Scientific Reports*, *6*(1), 37561. https://doi.org/10.1038/srep37561
Zhang, G. L., Zong, C. L., Yin, X. B., & Li, H. (2012). Geochemical constraints on a mixed pyroxenite–peridotite source for East Pacific Rise basalts. *Chemical Geology*, *330–331*, 176–187.
Zhang, L., Zhao, M. H., Wang, J., He, E. Y., Ao, W., Qiu, X. L., et al. (2013). Correction of OBS position and recent advances of 3D seismic exploration in the central sub-basin of South China Sea [in Chinese with English abstract]. *Earth Science Journal of China University of Geosciences*, *38*, 33–42.
Zou, H., & Fan, Q. (2010). U-Th isotopes in Hainan basalts, implications for sub-asthenospheric origin of EM2 mantle end member and the dynamics of melting beneath Hainan Island. *Lithos*, *116*(1–2), 145–152.